Extreme nonlinear dynamics of cantilever beams: effect of gravity and slenderness on the nonlinear modes

Marielle Debeurre · **Aurélien Grolet** · **Olivier Thomas**

Abstract In this paper, the effect of gravity on the nonlinear extreme amplitude vibrations of a slender, vertically oriented cantilever beam is investigated. The extreme nonlinear vibrations are modeled using a finite element discretization of the geometrically exact beam model solved in the frequency domain through a combination of harmonic balance and a continuation method for periodic solutions. The geometrically exact model is ideal for dynamic simulations at extreme amplitudes as there is no limitation on the rotation of the cross sections due to the terms governing the rotation being kept exact. It is shown that the very large amplitude vibrations of dimensionless beam structures depend principally on two parameters, a geometrical parameter and a gravity parameter. By varying these two parameters, the effect of gravity in either a standing or hanging configuration on the natural (linear) modes as well as on the nonlinear modes in extreme amplitude vibration is studied. It is shown that gravity, in the case of a standing cantilever, is responsible for a linear softening behavior and a nonlinear hardening behavior, particularly pronounced on the first bending mode. These behaviors are reversed for a hanging cantilever.

M. Debeurre (✉) · A. Grolet · O. Thomas
Arts et Métiers Institute of Technology, LISPEN, HESAM Université, 8 boulevard Louis XIV, Lille 59046, France
e-mail: marielle.debeurre@ensam.eu

A. Grolet
e-mail: aurelien.grolet@ensam.eu

O. Thomas
e-mail: olivier.thomas@ensam.eu

Keywords Nonlinear modes · Flexible cantilevers · Geometrical nonlinearities · Finite element analysis · Gravity effect

1 Introduction

This paper considers the extreme amplitude vibrations of cantilever beams with a focus on two particular effects: the influence of a gravitational field and that of the geometry of the cantilever, namely its slenderness. Slender beam structures are particularly susceptible to large amplitude vibrations because of the thinness of their cross section, which leads to a low bending stiffness and occasions large amplitude transverse vibrations for only moderate input forces. Moreover, in the special case of clamped-free boundary conditions, there is no restriction of the in-plane displacements (as in the case of a clamped-clamped beam, for instance) and, therefore, the oscillations can be extreme, especially near the first resonance of the structure. For example, the free end of the beam can be easily subjected to more than half of a complete turn, even reaching a state of bending "backwards" beyond the fixed end (see Fig. 4a and [1–4]). At large amplitudes of vibration, so-called geometrical nonlinearities (trigonometric terms related to the cross-section rotation) become consequential. Although at first glance the oscillations in such cases may seem highly complex, using the concept of nonlinear modes, it is possible to characterize the vibrations very easily in terms of oscillation fre-

quency and mode shapes. The purpose of this paper, then, is to address the effect of both gravity and the beam geometry on the nonlinear modes of cantilever beams, up to extreme amplitudes of vibration.

Past works in the literature on cantilever beam mechanics have investigated the effect of gravity on their static and dynamic behavior. In statics, Greenhill analyzed more than a century ago in [5] the point at which a tree, modeled as a "heavy column" cantilever, would buckle under its own weight, a phenomenon known as self-buckling. In dynamics, additional studies have investigated the influence of gravity on the free vibration of vertical cantilevers. An early study on the topic is found in the work of Paidoussis and Des Trois Maisons [6], who studied the influence of gravity on the free vibration of damped vertical cantilevers and recovered the self-buckling behavior described in [5]. In [7], Schäfer computed the effect of gravity on the eigenfrequencies of the first five modes of hanging Euler–Bernoulli cantilevers using a closed-form approximation based on the Ritz–Galerkin method for aerospace applications. The results of [7] were confirmed by the work of Yokoyama [8], where the eigenvalues were computed based on a finite element discretization of vertically hanging Timoshenko beams. Other studies on the free vibration of gravity-loaded beams include the work of Naguleswaran [9,10] and Bokaian [11,12] for Euler–Bernoulli-type cantilever beams, Abramovich [13] for composite Timoshenko-style hanging cantilevers and Xi et al. [14] for Rayleigh-type cantilevers. Naguleswaran, Bokaian and Xi et al. derived closed-form approximations of the natural frequencies of gravity-loaded cantilevers, while Abramovich estimated the eigenproblem using a Galerkin approach. In addition to these, Hijmissen and van Horssen [15] derived a closed-form approximation of the eigenfrequencies based on the linearized equations of motion of a vertical uniform Timoshenko cantilever using the method of multiple scales. This linear approximation is valid in particular for small effects of gravity. Furthermore, Virgin et al. experimentally investigated the influence of gravity on vertical cantilevers in [16,17] and, most importantly, validated experimentally in [17] the influence of gravity on the eigenfrequencies (e.g., Figure 2 in [14]) of the first four modes.

In all of these works, the primary interest was to investigate the influence of gravity on the linear eigenfrequencies of the vertical cantilevers. However, very little investigation has been done to date on the effect of gravity on the *nonlinear* dynamics of vertical cantilevers, especially at extreme amplitudes of vibration, which is the present aim of this paper. Santillan et al. derived an analytical perturbation approximation based on the elastica model for the first nonlinear mode of a standing cantilever including self-weight and compared the results with numerical finite difference results [18]. In [18], the authors also compared their backbone approximations to the analytical expression for the amplitude-vs-frequency relationship of cantilever beams derived by Luongo et al. [19], though this work did not include the effect of gravity. Finally, the recent work of Farokhi et al. [20] on the parametric response of cantilever beams at very large amplitudes of displacement discussed the strong influence of gravity on the nonlinear dynamic response of the system.

An appropriate beam model should be selected in order to properly capture the geometrical nonlinearities at very large amplitudes of vibration. In this paper, a finite element discretization of the geometrically exact beam model (also known as the Reissner–Simo beam model [21–25]), based on Timoshenko kinematics of the cross section, is used. The advantage of this model is that the geometrical nonlinearities are kept exact without any truncation or linearization, a strong advantage over other nonlinear models that break down at high amplitudes when the rotation of the cross section becomes large. An example of the latter is the widely used inextensible beam model of Crespo da Silva et al. [26,27], where the nonlinearities expanded in Taylor series were truncated at order three; this truncation begins to break down when the rotation of the cross section nears or exceeds $\pi/4$ rad. By contrast, the geometrically exact model remains exact at any amplitude of rotation, even beyond π rad, which is extreme in a standard vibration test.

The discretized geometrically exact beam model is then solved in the frequency domain using a combination of the harmonic balance method (HBM) and numerical continuation based on the asymptotic numerical method (ANM) to compute periodic solutions, a process developed in many previous works [28–32]. Although many works on the modeling of flexible beam structures using the geometrically exact model involve time domain strategies to solve the system [33–37] (as in commercial finite element codes), a solving technique based in the frequency domain has certain advantages. Solving in the frequency domain targets

the steady state of the periodic oscillations under harmonic forcing without needing to manage time steps or transient oscillations and also allows for easy bifurcation detection and stability analysis [32,38]. In this way, frequency domain strategies can target various complex nonlinear vibratory phenomena such as bifurcations, instabilities, energy transfer between modes (internal resonances) [39] and quasi-periodic or chaotic responses [40,41] that enrich the overall nonlinear dynamic analysis. Another set of works in the literature also used the geometrically exact model solved in the frequency domain to compute the dynamics of flexible cantilever beams [2,42] and later validated this model with experimental results, notably with the weight of the cantilever incorporated into the equations of motion in [42].

In this paper, we investigate the effects of gravity in both the linear and nonlinear regimes. For the latter, we are particularly interested in the effect of gravity on the nonlinear modes. Nonlinear modes provide a useful framework for understanding nonlinear vibrations as they constitute the skeleton of the nonlinear resonance pattern and can be useful in obtaining accurate reduced order models. Nonlinear modes are explicitly defined as families of periodic solutions of the system in free and undamped vibration [43], or as invariant manifolds of the phase space [38], both definitions being equivalent. In a way analogous to the eigenfrequencies and mode shapes in the linear regime, nonlinear modes are characterized by oscillation frequencies and mode shapes, which are dependent on the amplitude of the motion due to the presence of the nonlinearities, a point on which this article especially focuses in order to investigate the effect of gravity.

This paper is divided into five sections: In Sect. 2, the governing equations of motion are presented, including details on incorporation of the gravity terms. Section 3 discusses the effects of the gravity on the linear eigenfrequencies, including a comparison to the work of Hijmissen and van Horssen [15]. The nonlinear effects are treated in Sects. 4 and 5, with emphasis on computation of the nonlinear modes. Finally, the paper ends in Sect. 6 with an analogy to a simple pendulum system in order to provide a more physical interpretation of the effect of gravity on the cantilever system.

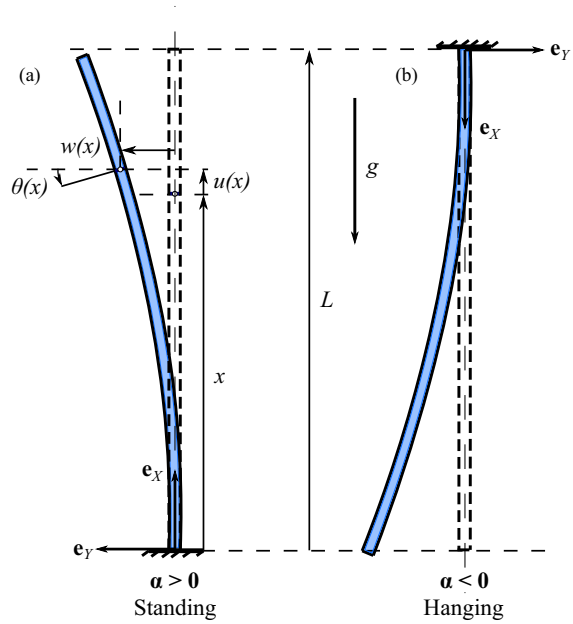

Fig. 1 Cantilever beam orientations with rectangular cross section: **a** standing configuration, **b** hanging configuration

2 Governing equations

In this section, the equations of motion and their finite element discretization are presented. Based on a previous work [44], the equations are here adapted to the case of a weighted cantilever. Within this framework, we begin by considering a straight cantilever beam of length L oriented vertically with respect to the direction of gravity, as shown in Fig. 1. Two orientations of the cantilever beam are equally considered: that of a *standing* cantilever, with the free end at the top of the beam (Fig. 1a), and that of a *hanging* cantilever, with the free end at the bottom (Fig. 1b).

2.1 Beam model

Based on Timoshenko beam kinematics, it is assumed that any cross section undergoes a rigid-body transformation that may be arbitrarily large. Considering that the undeformed centerline of the beam is aligned with the $\mathbf{e}_X$-direction and that the motion of the beam is restricted to the plane $(\mathbf{e}_X, \mathbf{e}_Y)$ of a global basis $(\mathbf{e}_X, \mathbf{e}_Y, \mathbf{e}_Z)$, the displacement field of any point in the cross section at location x along the beam in the refer-

ence (undeformed) configuration is written [44]:

$$\mathbf{u}(x, y, t) = [u(x, t) - y \sin\theta(x, t)]\,\mathbf{e}_X + [w(x, t) + y\,(\cos\theta(x, t) - 1)]\,\mathbf{e}_Y, \quad (1)$$

where (x, y) are the coordinates of the point of the beam in the reference configuration, t is the time, $u(x, t)$ and $w(x, t)$ represent, respectively, the axial and transverse displacements fields, and $\theta(x, t)$ is the total rotation of the cross section, including any shearing (see Fig. 1).

The strains are defined by the Green–Lagrange strain tensor, to which a consistent linearization is applied; in this process, the part of the strains relating to local strains is linearized, while the part relating to rigid-body rotation is kept exact (see [44] for more details). It is appropriate in cases where the local strains remain fairly small, as is true for our case of a very thin, slender beam structure, even for extremely large rotations of the cross section. The strains can then be written:

$$e = (1 + u')\cos\theta + w' \sin\theta - 1, \quad (2a)$$

$$\gamma = w' \cos\theta - (1 + u')\sin\theta, \quad (2b)$$

$$\kappa = \theta', \quad (2c)$$

with e and γ being the axial and shear strains, respectively, and κ the beam curvature, and where $\circ' = \partial \circ / \partial x$.

Following the derivations in [44], the strong form of the equations of motion is written:

$$\begin{cases} \rho A \ddot{u} = (N \cos\theta - T \sin\theta)' + n, & (3a) \\ \rho A \ddot{w} = (N \sin\theta + T \cos\theta)' + p, & (3b) \\ \rho I \ddot{\theta} = T(1 + e) - N\gamma + M' + q, & (3c) \end{cases}$$

with the generalized constitutive laws:

$$N = EAe, \quad T = kGA\gamma, \quad M = EI\theta', \quad (4)$$

where ρ, E, G are the density, Young's modulus and Coulomb's (shear) modulus, respectively, of the material, assumed homogeneous and isotropic, A and I are, respectively, the area and second moment of area of the cross section, and k is the shear correction factor that accounts for the non-uniformity of shear stresses in the cross section. The internal forces are denoted by N, T and M, the axial force, shear force and bending moment, respectively. They are linearly related to the strains according to a linear Kirchhoff–Saint–Venant constitutive law [45], which remains valid as long as the strains are small. The external forcing appears within n, p and q, which are, respectively, the axial force, transverse force and bending moment per unit length. Notice in Eq. (3) the geometrical nonlinearities $\sin\theta$ and $\cos\theta$ governing the rotation of the cross section, which are kept fully exact in the geometrically exact beam model.

For the cantilever beam under consideration, the boundary conditions are such that one end of the beam (at $x = 0$) is fixed and the other free (at $x = L$), written explicitly as:

$$u = w = \theta = 0, \qquad \text{at } x = 0, \quad (5a)$$

$$N = T = M = 0, \qquad \text{at } x = L. \quad (5b)$$

2.2 Dimensionless equations and independent parameters

The weight of the beam intervenes as a constant force in the direction of the gravitational acceleration vector. For the sake of this derivation, we choose as our reference configuration the standing beam (Fig. 1a), and thus, the gravitational acceleration is written $\mathbf{g} = -g\mathbf{e}_X$. Since n, p and q are expressed in material coordinates, gravity simply leads to an axial force $n = -\rho A g$.

To better understand the influence of the gravitational field on the beam Eq. (3) and to obtain independent parameters of the problem, it is convenient to render the system dimensionless. To do so, the system is normalized by injecting the following dimensionless parameters into the equations:

$$\bar{u}, \bar{w} = \frac{1}{L}(u, w), \quad \bar{x} = \frac{x}{L}, \quad \bar{t} = \frac{t}{L^2}\sqrt{\frac{EI}{\rho A}}, \quad \bar{\omega} = L^2\sqrt{\frac{\rho A}{EI}}\omega, \quad (6a)$$

$$\bar{N}, \bar{T}, \bar{q} = \frac{L^2}{EI}(N, T, q), \quad \bar{n}, \bar{p} = \frac{L^3}{EI}(n, p), \quad \bar{M} = \frac{L}{EI}M, \quad (6b)$$

where $\bar{(\,)}$ indicates a dimensionless parameter and L is a characteristic length, chosen here as the length of the cantilever. Injecting these dimensionless parameters into Eqs. (3) and (4) results in the following dimen-

sionless equations of motion:

$$\begin{cases} \ddot{\bar{u}} = (\bar{N}\cos\theta - \bar{T}\sin\theta)' - \alpha, & \text{(7a)} \\ \ddot{\bar{w}} = (\bar{N}\sin\theta + \bar{T}\cos\theta)' + \bar{p}, & \text{(7b)} \\ \eta\ddot{\theta} = \bar{T}(1+e) - \bar{N}\gamma + \bar{M}' + \bar{q}, & \text{(7c)} \end{cases}$$

with

$$\bar{N} = e/\eta, \quad \bar{T} = \gamma/\mu, \quad \bar{M} = \theta'. \tag{8}$$

It can be seen in the above equations that the system depends only on three independent parameters: η, μ and α, defined as:

$$\eta = \frac{I}{AL^2}, \qquad \mu = \frac{EI}{\mathrm{kGAL}^2} = \frac{2(1+\nu)\eta}{k},$$
$$\alpha = \frac{\rho g A L^3}{\mathrm{EI}} = \frac{\rho g L}{E\eta}, \tag{9}$$

where ν represents the material Poisson's ratio, with, for a homogeneous isotropic material, $G = E/[2(1+\nu)]$. Rewriting η for the case of a rectangular cross section as:

$$\eta = \frac{I}{AL^2} = \frac{bh^3/12}{bhL^2} = \frac{1}{12}\left(\frac{h}{L}\right)^2, \tag{10}$$

with h being the thickness of the cross section and b the width, η can be more easily interpreted as a slenderness parameter: the thinner the beam, i.e., the smaller the thickness-to-length ratio h/L, the smaller the η. The second parameter, μ, represents the ratio between the bending stiffness of the beam and its shear stiffness and is entirely related to the Timoshenko kinematics. In the case of Euler–Bernoulli kinematics, the shear stiffness would be infinite, leading to $\mu = 0$ and $\gamma = 0$. For a homogeneous and isotropic material, μ is a function of η, as shown above. For the special case of slender beams, both η and μ are very small (see Table 1).

Whereas parameters η and μ are common to any structure modeled as an assembly of beams (see, e.g., [4]), the effect of gravity appears solely in the equations through a new parameter, α, that can be interpreted as the ratio between the effect of the restoring force due to gravity and the one due to the bending stiffness. This parameter was previously introduced in the literature to explain the buckling of a standing cantilever under its own weight when exceeding the critical value $\alpha_{\mathrm{crit}} = 7.837$, as shown in [5].

Table 1 Thickness-to-length (h/L) ratio corresponding to different values of η for a rectangular cross section and $\mu = 2(1+\nu)\eta/k$, with $k = 5/6$ and $\nu = 0.3$

$\eta = \frac{1}{12}\left(\frac{h}{L}\right)^2$	h/L	μ
$2 \cdot 10^{-4}$	$0.0490 \simeq 1/20.4$	$6.24 \cdot 10^{-4}$
$1 \cdot 10^{-4}$	$0.0346 \simeq 1/28.9$	$3.12 \cdot 10^{-4}$
$5 \cdot 10^{-5}$	$0.0245 \simeq 1/40.8$	$1.56 \cdot 10^{-4}$
$1 \cdot 10^{-5}$	$0.0110 \simeq 1/91.3$	$3.12 \cdot 10^{-5}$
$1 \cdot 10^{-6}$	$0.0035 \simeq 1/289$	$3.12 \cdot 10^{-6}$
$1 \cdot 10^{-7}$	$0.0011 \simeq 1/913$	$3.12 \cdot 10^{-7}$
$1 \cdot 10^{-8}$	$0.0003 \simeq 1/2887$	$3.12 \cdot 10^{-8}$

Referring back to the definition of the gravitational acceleration vector $\mathbf{g}$ and Fig. 1, it can be seen that Eq. (7) apply also to the hanging beam configuration simply by changing the sign of g and, thus, the sign of α. Consequently, a standing cantilever configuration is obtained when $\alpha > 0$ and a hanging cantilever when $\alpha < 0$ as shown in Fig. 1; both cases will be considered in Sects. 3, 4 and 5.

Since the effect of gravity on the mechanics of the beam depends solely on the magnitude of α, it is worth analyzing in more detail the parameters that govern it. Returning to its definition in Eq. (9), it can be seen that α naturally increases linearly with the gravitational acceleration g. It also depends on the material characteristics of the beam through ρ and E, which is logical since α is related to the ratio between the weight of the beam and its bending stiffness. Finally, α depends on the geometry of the beam through L and η, indicating that the effect of gravity increases as the beam becomes more slender (i.e., as η decreases). For this reason, it is important to investigate both the effects of gravity (through α) and the slenderness (through η) on the beam mechanics. In this study, only slender beams will be considered, i.e., with very small η. We consider a maximum threshold ratio h/L of around $1/20$ for the beam to be considered very slender, meaning that $\eta \leq 2 \cdot 10^{-4}$ (see Table 1). The values of η selected in this paper are chosen accordingly, ranging between $\eta \in [10^{-8}, 2 \cdot 10^{-4}]$.

As seen above, μ conditions the shear stiffness of the beam and is very small for slender beams, being proportional to η. Apart from η, its value is governed by the Poisson's ratio $0 \leq \nu \leq 0.5$ and the shear coefficient k. The value of k itself depends on ν along with

the geometry of the cross section. It may be computed based on an energetic equivalence and roughly takes values between 0.8 and 0.9 (for rectangular cross sections, $k = 5/6 \simeq 0.833$) [46–48]. However, since only slender beams are considered in this article, the effect of shearing is, in fact, negligible and therefore virtually no difference between Timoshenko and Euler–Bernoulli kinematics is noticed. Consequently, the effect of variations in μ is not considered in what follows. (Values of $\nu = 0.3$ and $k = 1$ have been used in the simulations.) Instead, we consider that the principal parameters governing the behavior of the weighted cantilever are simply η and α. Additional analysis justifying this choice and further highlighting the minimal influence of shearing for the case of very slender beams is presented in Appendix A.

2.3 Finite element geometrically exact formulation

The problem under consideration here has been fully defined by Eqs. (3), (4) and (5). It is highly nonlinear due to the geometrical nonlinearities (the $\sin\theta$ and $\cos\theta$ terms) and has no closed-form solution in nonlinear dynamics. An approximate analytical solution, valid up to moderate rotations of the cross section, can be derived based on Euler–Bernoulli kinematics and assuming the condition of inextensibility and a third-order truncation of the nonlinearities (see Appendix C). However, as we concern ourselves more with extreme amplitude vibrations, we rely instead on a finite element (FE) method to discretize the spatial part of the problem. An alternate approach would have been to keep the model of Appendix C exact (i.e., without the third-order truncation), rewriting it solely as a function of the rotation of the cross section $\theta(x,t)$ and solving it via discretization on a mode shape basis, as done in [1,2].

The problem is discretized using standard finite elements with linear shape functions, as done previously in [4,44] without incorporating the effect of gravity, which is here added in. The beam is discretized into N^e two-node Timoshenko beam elements [49], each of length L^e, which could depend on x if the mesh is not uniform. The $(\,)^e$ superscript is used to differentiate quantities related to the individual elements from their global counterparts. For each node of the mesh, there are three degrees of freedom (u_i, w_i, θ_i), representative of the axial displacement, transverse displacement and rotation of the cross section, respectively. For each element, the degrees of freedom at each of the two nodes are gathered in the vector $\mathbf{q}^e$:

$$\mathbf{q}^e = \left[u_1 \; w_1 \; \theta_1 \; u_2 \; w_2 \; \theta_2\right]^{\mathrm{T}}, \tag{11}$$

which relates to the displacements interpolated over the element $\forall x \in [0, L^e]$ according to:

$$\begin{bmatrix} u^e(x,t) \\ w^e(x,t) \\ \theta^e(x,t) \end{bmatrix} = \mathbf{N}(x)\mathbf{q}^e(t), \tag{12}$$

where $\mathbf{N}$ is the matrix of shape functions for each element, defined as:

$$\mathbf{N}(x) = \begin{bmatrix} N_1(x) & 0 & 0 & N_2(x) & 0 & 0 \\ 0 & N_1(x) & 0 & 0 & N_2(x) & 0 \\ 0 & 0 & N_1(x) & 0 & 0 & N_2(x) \end{bmatrix}. \tag{13}$$

Since linear shape functions are used, N_1 and N_2 take the form:

$$N_1(x) = 1 - \frac{x}{L^e}, \quad N_2(x) = \frac{x}{L^e}. \tag{14}$$

The equations of motion of the finite element model are derived from the principle of virtual work, which is written, for all virtual displacement $\delta\mathbf{u}$:

$$\delta W_a + \delta W_i = \delta W_e, \tag{15}$$

with δW_a being the inertial, δW_i the internal and δW_e the external virtual works. Integrating Eq. (12), the virtual work terms are discretized in order to define the elementary mass matrix, the internal and external force vectors and any other elementary quantities for a single element (the explicit details of which, omitted here, are outlined in [4]).

The effect of gravity is introduced as an applied force in the external virtual work component δW_e, which is written:

$$\delta W_e^e = \int_{V^e} (\delta\mathbf{u})^{\mathrm{T}}\mathbf{b}\,\mathrm{d}V = \int_0^{L^e} \left(\delta u \; \delta w \; \delta\theta\right) \begin{pmatrix} n \\ p \\ q \end{pmatrix} \mathrm{d}x, \tag{16}$$

where $n(x,t)$, $p(x,t)$ and $q(x,t)$ correspond to the distributed axial force, transverse force and bending moment, respectively, as in Eq. (3), and where $\mathbf{b}$ is the vector of body forces. As explained in Sect. 2.2, gravity appears in the axial direction as $n = -\rho A g$, $p = q = 0$, which, integrating Eq. (12) into (16), leads to:

$$\delta W_e^e = \left(\delta \mathbf{q}^e\right)^{\mathrm{T}} \underbrace{\left(-\rho A g \int_0^{L^e} \mathbf{N}^{\mathrm{T}} \begin{bmatrix} 1 \\ 0 \\ 0 \end{bmatrix} \mathrm{d}x \right)}_{\mathbf{f}_{\mathrm{g}}^e}, \tag{17}$$

with:

$$\mathbf{f}_{\mathrm{g}}^e = -\frac{1}{2} \rho A g L^e \begin{bmatrix} 1 & 0 & 0 & 1 & 0 & 0 \end{bmatrix}^{\mathrm{T}}. \tag{18}$$

Following this, the expressions for the elementary quantities are assembled for the entire structure according to traditional finite element assembly procedures. Formally, the problem can be written:

$$\mathbf{M}\ddot{\boldsymbol{q}} + \mathbf{D}\dot{\boldsymbol{q}} + \mathbf{f}_{\mathrm{int}}(\mathbf{q}) = \mathbf{f}_{\mathrm{g}} + \mathbf{f}_{\mathrm{ext}}, \tag{19}$$

where $\mathbf{q}$ is the column vector containing all degrees of freedom u_i, w_i and θ_i, $i \in [1,\ N]$ with $N \in \mathbb{N}$ being the number of nodes, $\mathbf{M}$ is the mass matrix of size $3N \times 3N$, $\mathbf{f}_{\mathrm{int}}(\mathbf{q})$ is the internal force vector, $\mathbf{f}_{\mathrm{g}}$ is the gravitational force vector, and $\mathbf{f}_{\mathrm{ext}}$ is the external force vector (housing all external forces except gravity), all three of size $3N \times 1$. The geometrical nonlinearities $\sin\theta_i$ and $\cos\theta_i$ appear in the internal force vector $\mathbf{f}_{\mathrm{int}}$, the full expression of which is found in [4]. A linear damping term, with the damping matrix $\mathbf{D}$ of size $3N \times 3N$, is also introduced for the sake of generality, although this term is not used in what follows since we focus on free, undamped vibrations. Finally, considering the fixed-free boundary conditions defined by Eq. (5), a null value for degrees of freedom (u, w, θ) is enforced at the node located at $x = 0$.

2.4 Numerical solving and type of problems considered

As explained in the introduction, in this study we focus primarily on computation of the nonlinear modes of the system under the influence of gravity. Consequently, we consider the free and undamped problem associated with Eq. (19), namely:

$$\mathbf{M}\ddot{\boldsymbol{q}} + \mathbf{f}_{\mathrm{int}}(\mathbf{q}) - \mathbf{f}_{\mathrm{g}} = \mathbf{0}. \tag{20}$$

The nonlinear modes are here computed by continuation of periodic solutions as the families of periodic orbits that emerge from the equilibrium position of the system in the phase space. They are identical to the invariant manifolds of the system, as explained, e.g., in [38]. In practice, the harmonic balance method (HBM) is used to compute the periodic solutions of the problem as Fourier series of $\mathbf{q}(t)$. The HBM transforms Eq. (20) into an algebraic system, which is then solved by the asymptotic numerical method (ANM) in a process extensively documented in previous works [4,32]. Solving the system yields the evolution of the Fourier components of $\mathbf{q}(t)$ as a function of the frequency Ω of the oscillations, leading to the frequency/amplitude relations of the nonlinear modes, well known as the so-called backbone curves, as well as the nonlinear mode shapes. These are investigated in Sects. 4 and 5. As a final detail, it should be mentioned that since Eq. (20) is autonomous, a phase condition and a fictitious damping term are added for numerical purposes, as fully explained in [4].

Due to the presence of gravity, the equilibrium (static) configuration of the system is not $\mathbf{q}_{\mathrm{s}} = \mathbf{0}$ but the solution of:

$$\mathbf{f}_{\mathrm{int}}(\mathbf{q}_{\mathrm{s}}) - \mathbf{f}_{\mathrm{g}} = \mathbf{0}, \tag{21}$$

which is representative of an axial compression of the cantilever in the standing equilibrium configuration and to a stretching in the hanging configuration. The static solution is used in two different computations, either as the starting point for computation of the nonlinear modes or in computation of the evolution of the (linear) eigenmodes of the problem.

Since we are interested in vibrations of the system, it is convenient to consider its oscillations around the equilibrium configuration $\tilde{\mathbf{q}}(t)$, defined by:

$$\tilde{\mathbf{q}}(t) = \mathbf{q}(t) - \mathbf{q}_{\mathrm{s}}. \tag{22}$$

Introducing this equation into Eq. (20), the problem is rewritten for $\tilde{\mathbf{q}}(t)$:

$$\mathbf{M}\ddot{\tilde{\mathbf{q}}} + \mathbf{f}_{\mathrm{int}}(\tilde{\mathbf{q}} - \mathbf{q}_{\mathrm{s}}) - \mathbf{f}_{\mathrm{g}} = \mathbf{0}. \tag{23}$$

Equation (23) can be linearized using the Taylor expansion of $\mathbf{f}_{\text{int}}(\mathbf{q})$ around $\mathbf{q}_{\text{s}}$, yielding:

$$\mathbf{f}_{\text{int}}(\mathbf{q}) \simeq \mathbf{f}_{\text{int}}(\mathbf{q}_{\text{s}}) + \mathbf{K}_{\text{t}}(\mathbf{q}_{\text{s}})\tilde{\mathbf{q}}, \qquad \mathbf{K}_{\text{t}}(\mathbf{q}_{\text{s}}) = \left.\frac{\partial \mathbf{f}_{\text{int}}}{\partial \mathbf{q}}\right|_{\mathbf{q}=\mathbf{q}_{\text{s}}}, \tag{24}$$

where the nonlinear terms in the Taylor expansion have been neglected and with $\mathbf{K}_{\text{t}}$ being the tangent stiffness matrix. Introducing Eq. (24) into Eq. (20) and using Eq. (21), the following relation is obtained:

$$\mathbf{M}\ddot{\tilde{\mathbf{q}}} + \mathbf{K}_{\text{t}}(\mathbf{q}_{\text{s}})\tilde{\mathbf{q}} = \mathbf{0}. \tag{25}$$

This problem defines the small (linearized) oscillations of the system around its equilibrium (weighted) position, which leads to the eigenvalue problem:

$$\left[\mathbf{K}_{\text{t}}(\mathbf{q}_{\text{s}}) - \omega^2\mathbf{M}\right]\boldsymbol{\Phi} = \mathbf{0}. \tag{26}$$

The solutions of Eq. (26) are the (linear) eigenmodes $(\omega_m, \boldsymbol{\Phi}_m)$, $m = 1, \ldots N$ of the system. Since $\mathbf{q}_{\text{s}}$ is directly tied to gravity (Eq. (21)), the effect of the weight of the cantilever beam on its own eigenmodes can be analyzed by solving this eigenvalue problem. The results of this analysis are described in Sect. 3. In practice, the tangent stiffness matrix $\mathbf{K}_{\text{t}}$ is computed according to standard FE assembly procedures, a process explained in Appendix B.

Two different methods for computing $\mathbf{q}_{\text{s}}$ are implemented and compared. The first method computes the solution of the full nonlinear problem directly using a Newton–Raphson iteration algorithm to solve the nonlinear Eq. (21). A second method computes $\mathbf{q}_{\text{s}}$, which is assumed very small since the beams under consideration are very stiff in the axial direction, with the linearized version of Eq. (21), written:

$$\mathbf{K}_{\text{t}}(\mathbf{0})\mathbf{q}_{\text{s}} = \mathbf{f}_{\text{g}}. \tag{27}$$

It is noted that since $\mathbf{q}_{\text{s}}$ is typically small, the results of the two methods are virtually identical; however, some inconsistencies are uncovered when computing $\mathbf{q}_{\text{s}}$ for very small values of η (i.e., $\eta \leq 10^{-8}$), which is discussed in the next section (§3).

Moreover, recall from Sect. 2.2 that the system can be normalized by introducing the dimensionless parameters defined in Eq. (6). For better conditioning of the numerical problem and to bring more universality to the results, the normalized system is used in practice, simply by selecting the following values for the material and geometrical parameters of the system: $L = 1$, $EI = 1$, $\rho A = 1$, $\rho I = \eta$, $EA = 1/\eta$, $kGA = 1/\mu = k/[2(1+\nu)\eta]$ and $g = \alpha$. Since, as explained before, variations of μ are not investigated, values of $\nu = 0.3$ and $k = 1$ are selected in the simulations. Finally, all numerical computations presented in this work are carried out on a finite element mesh of $N = 50$ nodes (i.e., 49 elements) and with $H = 20$ harmonics in the HBM computations.

3 Effect of (α, η) on the natural frequencies

In this section, the effect of gravity on the (linear) natural frequencies of the (dimensionless) system is investigated. Following the discussion of Sect. 2.2, only two independent parameters condition the mechanics of the beam: the slenderness parameter η and the gravity parameter α. In order to investigate first the effect of (α, η) on the natural frequencies, the beam's parameters are chosen as explained at the end of Sect. 2.4 and the modes of the beam $(\bar{\omega}_m, \boldsymbol{\Phi}_m)$ are computed by numerically solving Eq. (26) for several values of (α, η). Throughout this work, we choose to concentrate on the first three bending modes of the cantilever beam, $m = 1, 2, 3$.

The results of the effect of (α, η) on $\bar{\omega}_m$ are summarized in Fig. 2a for the first three bending modes. For reference, the deformed shape of the first bending mode is depicted in Fig. 3a, while the second and third bending modes are depicted in Fig. 3b and c. The linear natural frequencies $\bar{\omega}_m$ for $m = 1, 2, 3$ are solved for a range of α values for six different η values (six different beam geometries). The black dashed line at $\alpha = 0$ indicates the location of zero gravity (i.e., where the weight of the beam is not taken into account), with negative α to the left indicating a "hanging" beam configuration and positive α to the right indicating a "standing" beam. At the point of "no gravity" ($\alpha = 0$), the value of $\bar{\omega}_m$ for each mode matches its classical dimensionless natural frequency for a uniform cantilever beam [50] ($\bar{\omega}_m = [3.516, 22.034, 61.701]$ for $m = 1, 2, 3$). In addition, Fig. 2b shows a zoom of Fig. 2a onto the first bending mode.

First, consider the effect of η on $\bar{\omega}_m$. The computation of $\bar{\omega}_m = f(\alpha)$ is performed for six different values

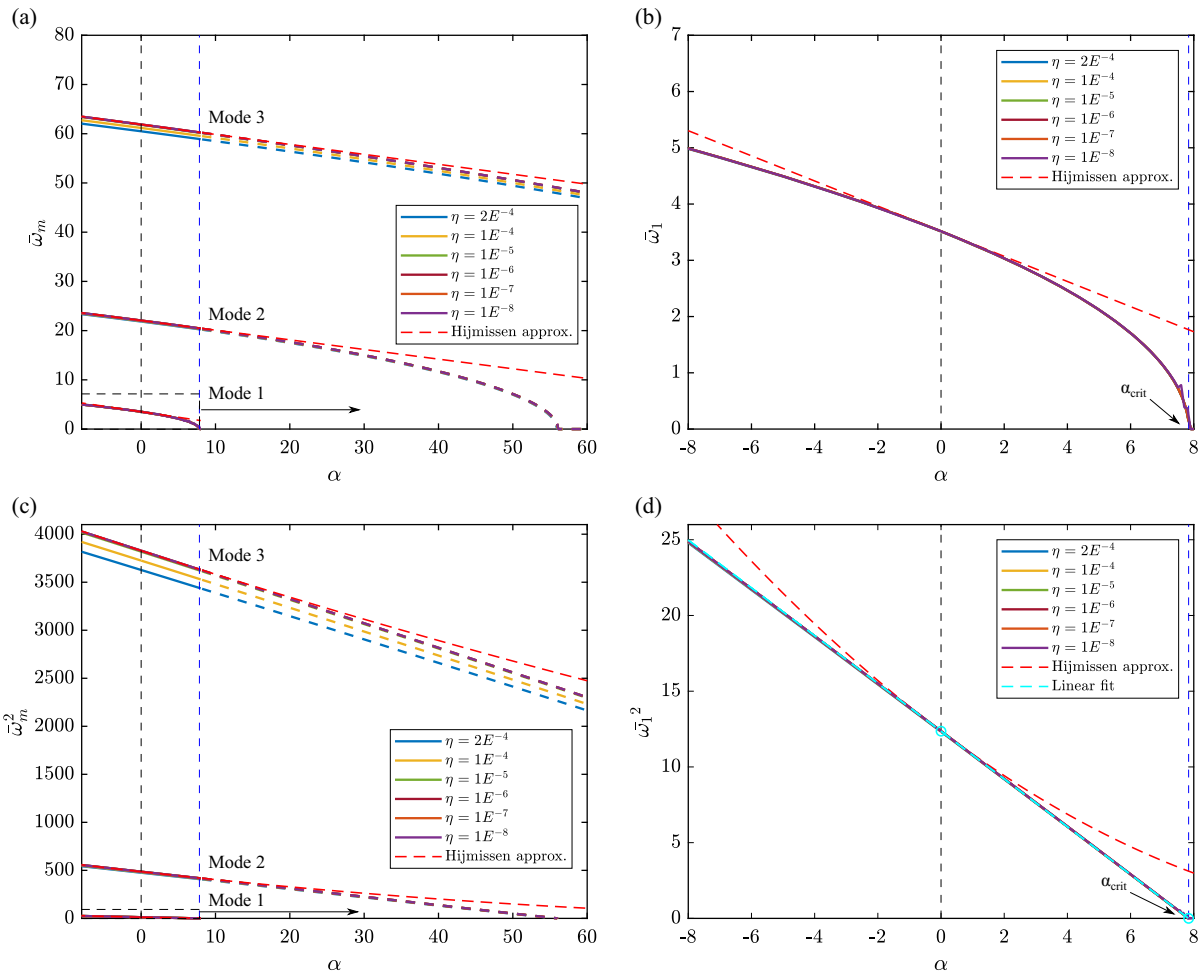

Fig. 2 Effect of gravity on the dimensionless natural frequencies $\bar{\omega}_m$: **a** for the first three bending modes of the cantilever beam, **b** zoom of **a** onto the first bending mode, **c** the same as **a** but depicting $\bar{\omega}_m^2 = f(\alpha)$, **d** zoom of **c** onto the first bending mode. Several values of the slenderness parameter η as well as approximations based on [15] are depicted, as specified in the legend. The vertical blue dashed lines indicate the self-buckling point at α_{crit}. A linear fit based on the two points indicated with circles in **d** is shown in cyan

of η ranging from $2 \cdot 10^{-4}$ to 10^{-8}, i.e., from a rather thick beam to a very thin one (see Table 1 for the values of h/L corresponding to η in the case of a rectangular cross section). In Fig. 2a, it is readily seen that, for all three modes, $\bar{\omega}_m = f(\alpha)$ varies little for different values of η. In fact, there is virtually no difference in the curves apart from on the third bending mode, where an $\eta = 2 \cdot 10^{-4}$ or 10^{-4} reduces $\bar{\omega}_3$ slightly compared to other η. (Some discussion on the larger effect of η on mode 3 is presented at the end of Sect. 4.1.) It can be said, then, that the effect of η for $\eta \leq 10^{-5}$ on the natural frequencies $\bar{\omega}_m$ is negligible.

The same cannot be said for the influence of α on $\bar{\omega}_m$. Particularly on the first mode of vibration, $\bar{\omega}_1$ changes significantly for different values of α. In general, for all three modes, a negative α increases the natural frequency, while a positive α decreases it. The effect of gravity on a standing (resp. hanging) cantilever is to add a restoring force in the system which acts qualitatively in the same way as a pre-compression (pre-tension). This pre-compression (pre-tension) of the beam results in a decrease (increase) of the bending stiffness and, thus, decreases (increases) the natural frequencies. A more physical interpretation of this

effect can be described using a simple pendulum system, which is explained in detail in Sect. 6. In the case of the standing cantilever ($\alpha > 0$), the gravity decreases the global bending stiffness of the cantilever until it is completely canceled, which occurs at a critical value of the gravity parameter $\alpha = \alpha_{\text{crit}} = 7.837$. In statics, α_{crit} corresponds to the point of self-buckling, well known in the literature [5], at which the standing beam buckles under its own weight. In dynamics, α_{crit} corresponds to the first natural frequency $\bar{\omega}_1$ tending to zero [51–53], as shown in Fig. 2b. Beyond the point of self-buckling, the compressed, straight and vertical equilibrium configuration of the beam is no longer stable, indicated by the dashed portions of the mode 2 and 3 curves in Fig. 2a. The dashed blue line in Fig. 2 indicates the location of failure due to self-buckling at α_{crit}.

Note, however, that as α approaches α_{crit}, the linearized tangent stiffness matrix $\mathbf{K}_{\text{t}}$ approaches a singularity, which occurs exactly at the self-buckling point (at $\alpha = \alpha_{\text{crit}} \Leftrightarrow \bar{\omega}_1 = 0$). This effect is explained since the terms in $\mathbf{K}_{\text{t}}$ related to the bending stiffness are decreased (and canceled at $\alpha = \alpha_{\text{crit}}$) due to the influence of gravity. This effect is magnified when η is very small, which explains the numerical noise observed in the $\bar{\omega}_1 = f(\alpha)$ curve of Fig. 2b close to the buckling point when $\eta = 10^{-8}$. For very small values of η (observed in our case only for $\eta = 10^{-8}$), the linear computation of $\mathbf{q}_{\text{s}}$ using Eq. (27) is not considered sufficiently accurate due to the existence of this numerical noise in the $\bar{\omega}_1 = f(\alpha)$ curve. To avoid this, the nonlinear computation of Eq. (21) is used, although some numerical noise remains very close to α_{crit}.

In the stable equilibrium region $\alpha < \alpha_{\text{crit}}$, it can be seen that α does not have as strong of a relative influence on $\bar{\omega}_m$ for $m > 1$. To describe this effect quantitatively, compare the values of $\bar{\omega}_m$ at $\alpha = 0$ and $\alpha = 7$ for all three modes: at $\alpha = 0$, $\bar{\omega}_m = [3.51, 21.93, 61.03]$ and at $\alpha = 7$, $\bar{\omega}_m = [1.18, 20.64, 60.44]$ for $m = 1, 2, 3$, respectively. On modes 2 and 3, $\bar{\omega}_m$ decreases by less than 6% and 1%, respectively, while on mode 1, it decreases by more than 66% between $\alpha = 0$ and $\alpha = 7$. This simple comparison highlights the large influence of the gravity parameter α on the natural frequency of the first bending mode of vibration of the cantilever beam, while its influence remains relatively small on higher-frequency bending modes. The same was found in the work of Hijmissen and van Horssen in [15]; computing their linear estimation of $\bar{\omega}_m = f(\alpha)$ for $m = 1, 2, 3$ revealed a weaker α influence on the higher-frequency modes. The linear estimations provided by Hijmissen and van Horssen [15] are given by the red dashed lines in Fig. 2a for comparison, again with a zoom on the first mode in Fig. 2b. Our results are in good agreement with the estimation of [15] (particularly close to $\alpha = 0$), once again highlighting the strong influence of α on $\bar{\omega}_1$.

An interesting feature can be seen when plotting $\bar{\omega}_m^2$ as a function of α, as done in Fig. 2c and d: It is observed that an almost linear relationship exists between the square of the natural frequencies and α, a trend likewise noticed in [17]. A linear fit through the two known points $\left(0, \bar{\omega}_{0,1}^2\right)$ and $(\alpha_{\text{crit}}, 0)$ is overlaid onto Fig. 2d to further highlight this, where $\bar{\omega}_{0,m} = \bar{\omega}_m(\alpha = 0)$. By consequence, a good approximation of the α dependence of the natural frequencies can be written as a square root relationship:

$$\bar{\omega}_m = \bar{\omega}_{0,m}\sqrt{1 - \alpha/\alpha_{\text{cr},m}}, \tag{28}$$

where $\alpha_{\text{cr},m}$ is the m-th buckling point, with of course $\alpha_{\text{cr},1} = \alpha_{\text{crit}} = 7.837$. This relationship explains why α has a stronger influence on $\bar{\omega}_1$ than on the higher-frequency modes: Considering the particular shape of the square root, each curve $\bar{\omega}_m = f(\alpha)$ is a scaled version of the same overall shape, with a breakdown at $\alpha = \alpha_{\text{cr},m}$ (see Fig. 2a). Consequently, $\bar{\omega}_1 = f(\alpha)$ decreases more in the range $\alpha \in [0\ \alpha_{\text{cr},1}]$ than the higher natural frequencies $\bar{\omega}_m$, $m > 1$, justifying the stronger effect of α on $\bar{\omega}_1$.

4 Effect of (α, η) on nonlinear backbone curves

Next, we turn to the effects of gravity on the *nonlinear* dynamics of the slender cantilever beam. When the displacement of the beam becomes sufficiently large, the geometrical nonlinearities (recall Eqs. (2) and (3)) are activated. As explained in the introduction, in this paper we choose to focus on the nonlinear modes of the cantilever, represented here by their backbone curves and nonlinear mode shapes. The nonlinear modes are defined as the particular solutions of the undamped and free oscillation problem, defined here by Eqs. (20) or (23). Note that they share this definition with the standard (linear) eigenmodes of a linear system, the difference being the nonlinearities in the equations of motion. They correspond equivalently to invariant manifolds of

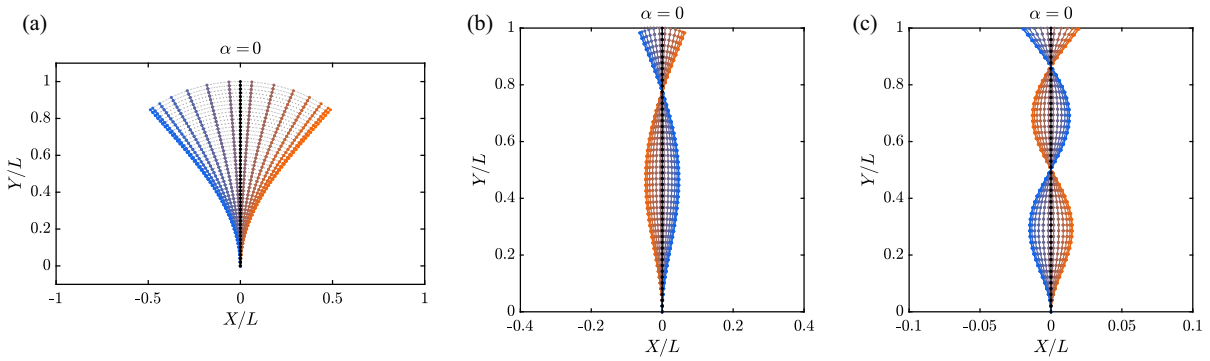

Fig. 3 Snapshots of the cantilever beam vibrating on its first three nonlinear modes at moderate amplitude: **a** first mode, **b** second mode, **c** third mode. The locations on the backbones at which the snapshots are taken are marked with black circles in Figs. 5, 6, 8a and 9

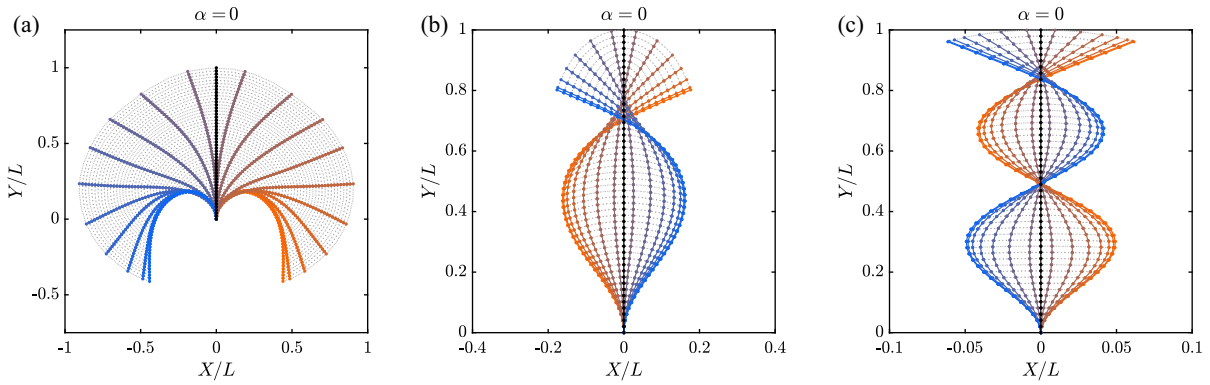

Fig. 4 Snapshots of the cantilever beam vibrating on its first three nonlinear modes at high amplitude: **a** first mode, where the cantilever has "bent backwards" beyond its fixed end, **b** second mode, **c** third mode. The locations on the backbones at which the snapshots are taken are marked with blue circles in Figs. 5, 6, 8a and 9

the phase space or to families of periodic solutions (see, e.g., [38]). The latter (families of periodic solutions) definition is used here to compute the nonlinear modes with the HBM-ANM strategy. The main difference with linear modes is that the free oscillation frequency and the shape of the motion on the mth nonlinear mode—the extension of the natural frequencies ω_m and the mode shape $\mathbf{\Phi}_m$ to the nonlinear regime—now depend on the amplitude (or energy) of the motion. The former is represented here in a classical amplitude/frequency plot called the *backbone curve*. The latter, the nonlinear mode shape, depends on the amplitude and is illustrated by plotting snapshots of the beam oscillations over a half period, at a given energy. Examples for the first mode are shown in Figs. 3a and 12 for low-to-moderate amplitudes of vibration and in Fig. 4a at very large amplitude. The second and third mode shapes are shown in Fig. 3b and c at moderate amplitude and in Fig. 4b and c at a higher amplitude. In this section, we focus on the effect of (α, η) on the backbone curves; the effect on the nonlinear mode shapes is addressed in Sect. 5.

As before, the influences of the two dimensionless parameters α and η are studied separately. To this end, the backbone curves are computed by solving Eq. (20) with the HBM-ANM method for several values of (α, η). Results are presented in Sect. 4.1 for constant α and in Sect. 4.2 for constant η. Here, the backbone curves trace the evolution of the amplitude of the first harmonic (H1) of either the cross-section rotation at the free end of the cantilever $\theta(L, t)$ or the transverse displacement $w(L, t)$ as a function of the frequency

of oscillation Ω ($\Omega = 2\pi/T$ with T the period of the motion) in Figs. 5, 6, 8 and 9. Based on the results of [1,4], it was found that showing only H1 gives an excellent image of the amplitude of the periodic solution since this harmonic is heavily dominant up to very large amplitudes of displacement. Moreover, the backbone curves tied to the cross-section rotation $\theta(L,t)$ are considered more readable than those of the transverse amplitude $w(L,t)$ since they increase monotonically, whereas the latter fold at large amplitude, i.e., beyond $\theta(L,t) > \pi/2$ when the beam bends backwards (compare Fig. 5a and b). For this reason, mostly $\theta(L,t)$ backbones are depicted in this work, instead of $w(L,t)$. Note also that all backbone curves have been normalized by the (linear) natural frequency $\omega_m(\alpha)$, which depends on gravity, as analyzed in Sect. 3.

4.1 Effect of η

First, we study the isolated effect of the dimensionless slenderness parameter η on the first three nonlinear modes. In this case, the effect of gravity is removed, i.e., α is fixed at 0. The amplitude of the first harmonic H1 backbone curve is traced for the rotation degree of freedom θ at the free end of the cantilever, i.e., the location of maximum displacement on a cantilever beam, for several values of η. The θ backbone curve is shown for nonlinear modes one, two and three in Figs. 5a and 6. To these is also added the backbone curve of the first nonlinear mode for the transverse displacement degree of freedom $\bar{w}$ at the tip of the beam in Fig. 5b.

Beginning with the first nonlinear mode, the shape of the backbone curves in Fig. 5 highlights several classical phenomena in the field of nonlinear dynamics. First, it is seen that as the displacement amplitude of the vibrating cantilever increases, the oscillating frequency Ω/ω_1 likewise increases. This behavior is known as frequency dependence on the vibration amplitude and is strictly a nonlinear effect. (A linear "backbone" curve would be a straight vertical line at the resonant frequency.) If the frequency increases with increasing amplitude, the trend is referred to as *hardening* (versus *softening* if reversed). All backbone curves in Fig. 5 for different values of η depict this hardening trend, which validates the known hardening of the first nonlinear mode of the cantilever beam [2,42,44,54]. Another classical nonlinear effect is seen in the jumps and branches or "offshoots" from the main backbone curve. Such instances represent locations of internal resonance (IR), when some energy is transferred from one mode to another one because of a frequency locking between the harmonics of the oscillating mode and the nonlinear frequencies of other modes (see, *e.g.,* [38,43,55]).

The appearance of internal resonance points along the backbone curve can take different forms and can sometimes be challenging to compute numerically. For the present case of a cantilever beam, this was discussed in [4]. Furthermore, since the focus in this article centers on the main backbone curves, the IR branches are not computed entirely, leading in some cases to interruptions in the curve shown (as explained in [4]). Note that the shape of the backbone curves in Fig. 5 is slightly different from those shown in [4], especially in the vicinity of the IRs as well as at large amplitude. This is due to the fact that in [4], the maximum amplitude over one period of oscillation—thereby including the effect of all harmonics—was shown, whereas, here, only the amplitude of the first harmonic is depicted. However, the difference between the maximum amplitude and the first harmonic of θ is, in this case, slight; as mentioned earlier, the first harmonic greatly dominates the higher harmonics, which become consequential only at higher amplitude. This is illustrated in Fig. 7, which superimposes the backbone curve in terms of the maximum amplitude of $\theta(L,t)$ over one period onto the backbone curves of the first three odd harmonics H1, H3 and H5, and in which the dominance of H1 is clearly visible. Moreover, since the oscillations of the structure are symmetrical, $\theta(x,t)$ is an odd function of t and its even harmonics are zero (and, thus, are not included in Fig. 7). Some differences between [4] and this work can also be explained by the differences in the number of finite elements (FEs) and harmonics H. The number of FEs greatly influences the values of the natural frequencies of the higher modes and thus the locations of the IRs on the main branch, which is itself much less affected. A greater number of FEs also increases the number of IRs since it increases the number of natural modes and therefore the number of possible frequency lockings, which is also influenced by the number of harmonics H retained in the HBM. We use 50 FEs in the present article, whereas between 20 and 30 (depending on the mode) were used in [4], with the same number ($H = 20$) of harmonics in both cases. In practice, the IR branches are avoided during the continuation process by manually jumping across their zone of appear-

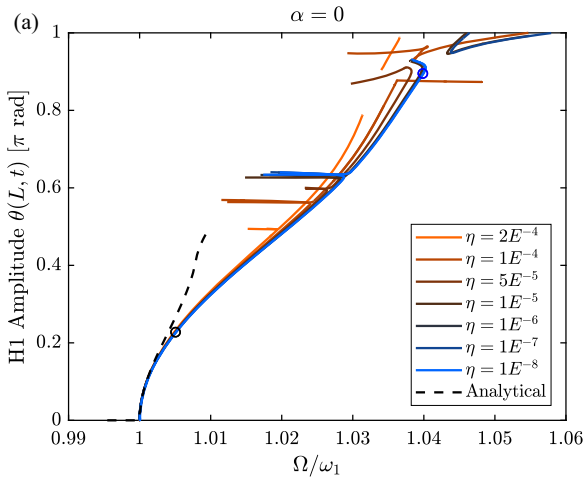

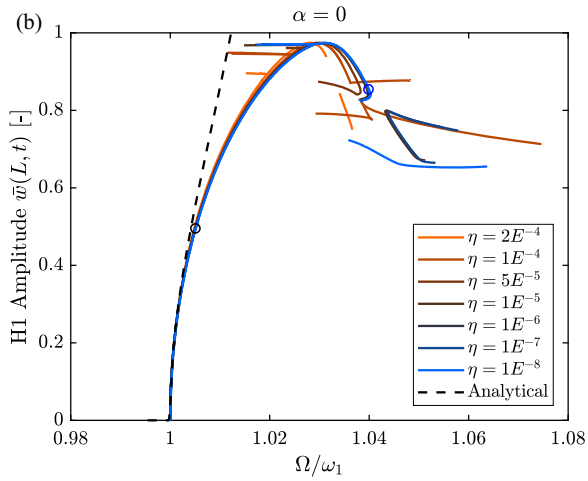

Fig. 5 Effect of the slenderness parameter η on the first nonlinear mode: **a** amplitude of the first harmonic H1 of θ at the free end of the beam for different values of η and comparison with inextensible (analytical) beam model [26,27], **b** amplitude of the first harmonic H1 of $\bar{w}$ at the free end of the beam for different values of η. Case with no gravity ($\alpha = 0$)

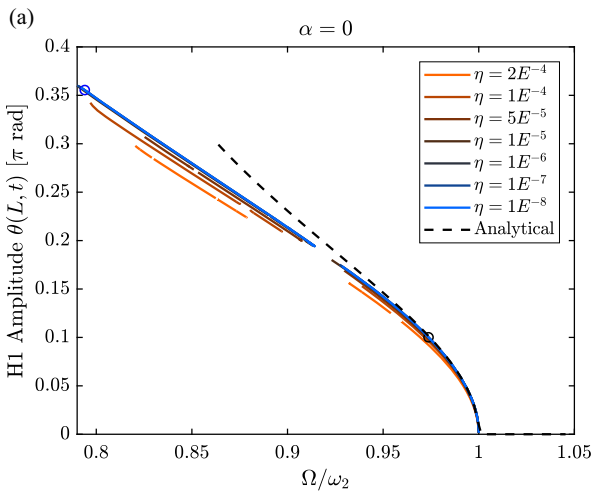

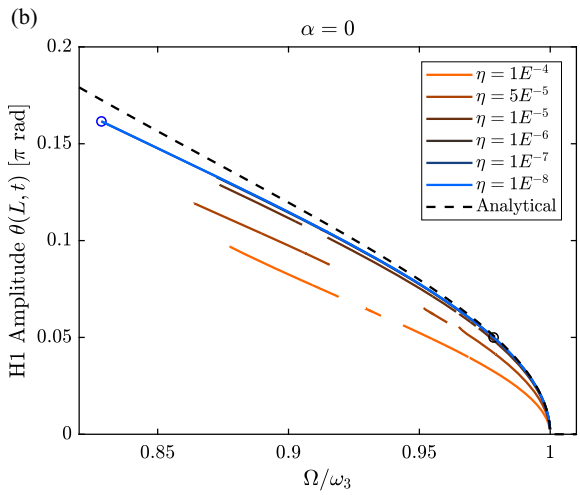

Fig. 6 Effect of the slenderness parameter η on the second and third nonlinear modes: **a** amplitude of the first harmonic H1 of θ at the free end of the beam for different values of η (mode 2) and comparison with inextensible (analytical) beam model [26,27], **b** the same as (a) for mode 3. Case with no gravity ($\alpha = 0$). Note that some curves (particularly for small η) overlap others and therefore some curves may not be visible

ance using an initial guess in frequency after the critical region and a Newton–Raphson algorithm to initiate the computation on the next branch. In the present case of a cantilever beam, this process is found to be delicate because some unusually large frequency ranges for the IR branches are uncovered: Notice the IRs around $\Omega \simeq 1.04\omega_1$ for the first mode and $\Omega \simeq 0.92\omega_2$ for the second mode in Fig. 7a and b). For the latter case, as shown in Fig. 7b, it is even more unusual that the branch of the first harmonic (dark blue) is virtually unaffected by the presence of the IR, meaning it can go undetected during continuation unless the third harmonic (brown) or the maximum amplitude of the periodic solution (light blue) is also monitored.

As in Sect. 3 for the natural frequencies, it can be seen that the effect of η on the mode 1 backbone curves

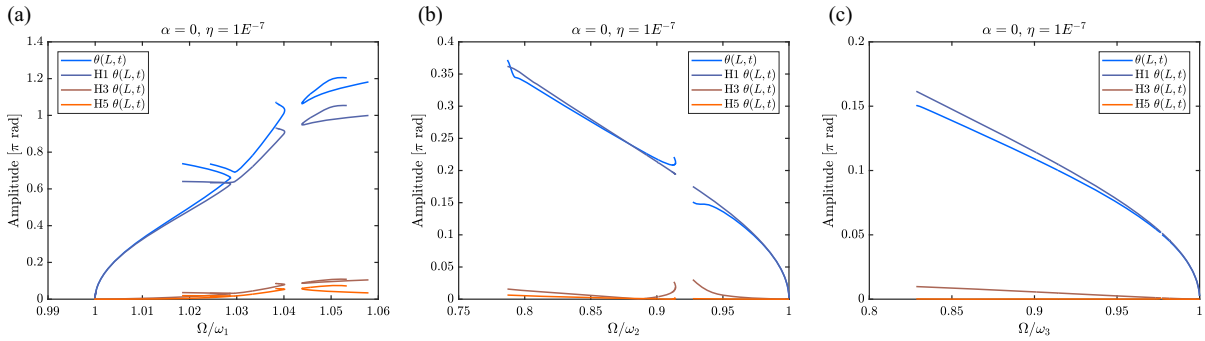

Fig. 7 Comparison of the maximum amplitude of $\theta(L,t)$ over one period of oscillation on the first three nonlinear modes with the amplitudes of the first three odd harmonics H1, H3 and H5. Note that the H1 curves are the same as those shown in Figs. 5 and 6 for $\alpha = 0, \eta = 10^{-7}$: **a** first nonlinear mode, **b** second, **c** third

(Fig. 5) is very slight, almost indistinguishable, so long as η remains small ($\eta \leq 10^{-5}$). The effect of η on the backbone curves becomes apparent only for larger values of η, i.e., when the beam is less slender. In this case, the location of the internal resonances shifts slightly due to changes in the frequencies of the higher modes that are affected by the change in η, thus moving the frequency locking. An analytical computation of the backbone curves is also included in Fig. 5, depicted with the dashed black curve, based on the approximate inextensible beam model of [26,27] restricted to the first bending mode (see Appendix C for details on this model). In this model, the geometrical nonlinearities are truncated in the Taylor series expansions at order 3 in w/L, leading to this model being valid only up to moderate amplitudes of vibration and diverging from the numerical (i.e., geometrically exact) backbone curves (around $\theta = 0.2\pi$ rad and $w = 0.5\,L$ at the beam's tip). This model is included in order to validate the finite element discretization of the geometrically exact model used here at low-to-moderate amplitudes.

For the second nonlinear mode, the same two observations as for mode 1 are made, as shown in Fig. 6a: the influence of η on the backbone curve is negligible, so long as η remains small ($\eta \leq 10^{-5}$), and also the backbone curve is validated at low amplitudes by the mode 2 inextensible model of Crespo da Silva et al. (Appendix C). The same cannot be said for the third nonlinear mode. As shown in Fig. 6b, the global trend of η's influence diminishing for small values of η holds, but only for *very* small η, around $\eta \leq 10^{-6}$. The influence of the slenderness of the beam seems to be quite large on the third nonlinear mode for "larger" η, e.g., $\eta > 10^{-5}$, even greater than on the first nonlinear mode. The mode 3 backbones for small $\eta \leq 10^{-6}$ are again validated by the inextensible analytical backbone, but these results seem to suggest a greater influence of the h/L ratio on the third nonlinear mode than on either of the first two. This trend seems logical when considering the mode shapes of the structure (see Fig. 3); an "improved" definition of the slenderness ratio η would consider instead h/λ_m, with λ_m a fraction of L representing the wavelength of the mode. Referring to Fig. 3 and according to the "improved" definition, as the mode number m increases, λ_m decreases, thereby suggesting a greater influence of η on the backbone curves of the higher modes. It is for this reason also that only η in the range of $[10^{-8}, 10^{-4}]$ is plotted for mode 3 in Fig. 6b.

4.2 Effect of α

Next, we investigate the influence of the dimensionless gravity parameter α on the first three nonlinear modes/backbone curves of the cantilever. A constant $\eta = 10^{-7}$ is selected, and the H1 backbones for the rotation degree of freedom θ at the free end of the beam (analogous to the backbones in the previous section) are shown as a function of the normalized frequency Ω/ω_m for different values of α. The results are summarized for mode 1 in Fig. 8 and for modes 2 and 3 in Fig. 9. Note that the mode 1 backbone for $(\alpha, \eta) = \left(0, 10^{-7}\right)$ is the same in both Fig. 5a and Fig. 8.

Beginning with the first nonlinear mode, as in Sect. 3, it can be seen that the dimensionless gravity parameter α has a significant effect on the backbone

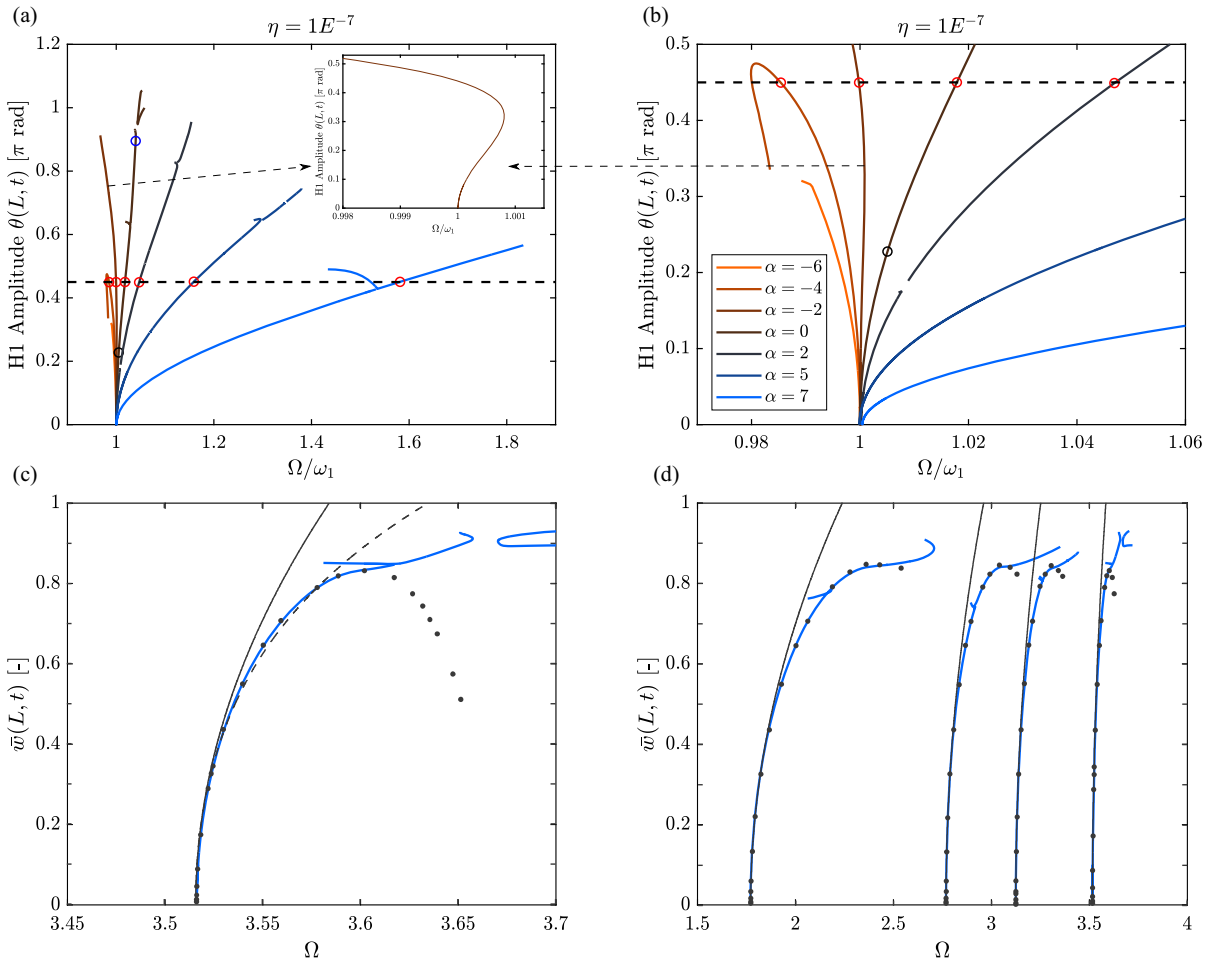

Fig. 8 Effect of dimensionless parameters on first nonlinear mode, isolation of the effect of α: **a** amplitude of the first harmonic H1 of θ at the free end of the beam for different values of α with inset zoom onto hardening-to-softening behavior for $\alpha = -2$, **b** a zoom of **a** at low amplitudes. Comparison ($\eta = 10^{-7}$) with results of Santillan et al. [18] and Luongo et al. [19]: **c** maximum transverse displacement of the free end over one period of oscillation for $\alpha = 0$ (solid black curve: perturbation approximation [18], dashed curve: finite differences [18], dots: analytical approximation [19], solid blue curve: $\eta = 10^{-7}$ backbone curve of Fig. 5), **d** the same as (c) but for (from left to right) $\alpha = 5.859, 2.989, 1.655, 0$

curve, much more of an effect than η in Sect. 4.1. It can be seen that, noting that the $\alpha = 0$ backbone is already of hardening type, increasing α in a standing configuration (i.e., increasing positive α) drastically hardens the backbone curve. In a similar way, decreasing α in a hanging configuration (i.e., decreasing negative α) softens the backbone curve, until it eventually becomes a globally softening backbone instead of the classical hardening mode 1 backbone. Notice in the inset of Fig. 8**a** that the backbone curve for $\alpha = -2$, which is globally of softening type, is initially of hardening type, before switching direction around $\theta = 0.35\pi$ rad. A softening-to-hardening transition of the backbone curve is classical for initially curved structures (see, e.g., [56,57] for shallow shells, [58–60] for shallow arches or [61] for curved cantilevers). However, an example of the hardening-to-softening transition like that of the $\alpha = -2$ backbone in Fig. 8 is much more uncommon, but was observed on the second nonlinear mode of a flexible ring structure in [4]. In addition, a comparison is made to the backbone approximations of Santillan et al. [18] and Luongo et al. [19] as shown in [18] for cantilever boundary conditions. In Fig. 8c, the maximum transverse displacement at the free end of the beam over one period for the $\eta = 10^{-7}$ backbone of Fig. 5 is computed and com-

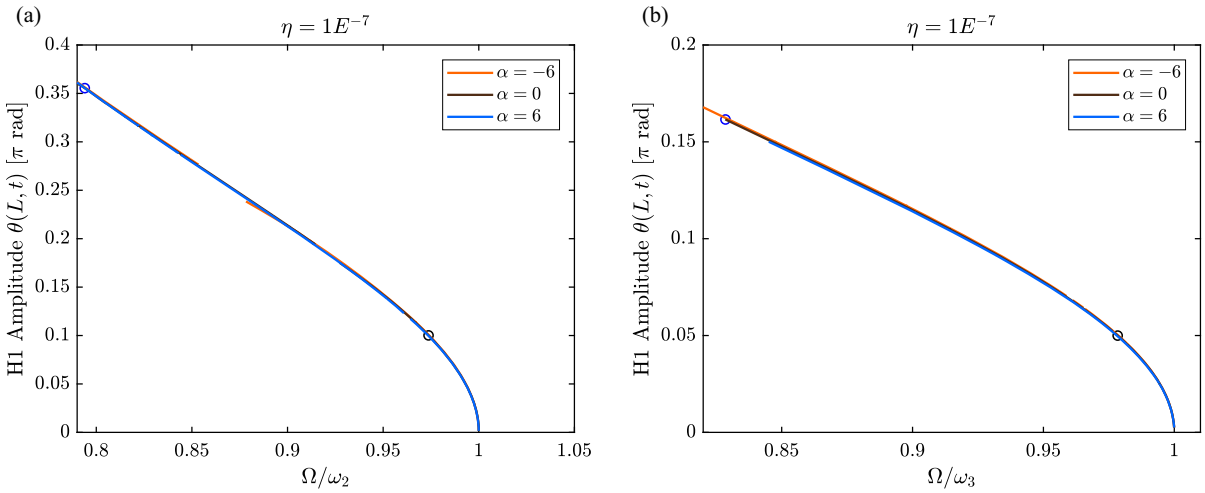

Fig. 9 Effect of dimensionless parameters on second and third nonlinear modes, isolation of the effect of α: **a** amplitude of the first harmonic H1 of θ at the free end of the beam for different values of α (mode 2), **b** the same as **a** for mode 3

pared to Fig. 5 of [18]. Likewise, the same comparison is carried out for Fig. 7 of [18] for three nonzero values of $\alpha = [1.655, 2.989, 5.859]$ in Fig. 8d. Up to very high amplitudes, it can be seen that there is excellent agreement between our results and the finite differences computation of [18]. The differences at high amplitude are probably due to the time integration method used in [18], which did not enforce periodicity of the response (or invariance), the property used here to compute the nonlinear modes.

With regard to the second and third nonlinear modes, the H1 backbone curves for the same θ degree of freedom at the free end of the beam as for mode 1 are shown for several values of α in Fig. 9a for mode 2 and 9b for mode 3. It can be seen that gravity has only a very minor influence on the backbone curves, almost unnoticeable. It is for this reason that only a few very different values of $\alpha \in \{-6, 0, 6\}$ are selected for modes 2 and 3 prior to the self-buckling occurring at $\alpha_{\text{crit}} = 7.837$, where $\alpha = 6$ can be considered as a "large" effect of gravity on a physical standing cantilever.

Finally, the joint effect of η and α on the nonlinear modes is studied, where η is varied while including the effect of gravity, i.e., $\alpha \neq 0$. On the first nonlinear mode, η is varied as in Fig. 5 for $\alpha = 7$ and $\alpha = -2$, this latter case being selected in particular due to the unique hardening-to-softening transition of the backbone curve observed in Fig. 8. On the second and third nonlinear modes, η is varied for $\alpha = 6$ and $\alpha = -6$ in order to be consistent with Fig. 9. The results are summarized in Fig. 10 for the first nonlinear mode and in Fig. 11 for the second and third nonlinear modes. In general, the main conclusions already established for the ranges of η and α studied in this work hold also for $\eta, \alpha \neq 0$, namely that η does not have a strong influence on the backbone curves no matter the value of α so long as η is small, and that α has a strong influence only on the first nonlinear mode. Interestingly, however, larger values of η ($\eta > 10^{-5}$) appear to have a greater influence on the first nonlinear mode as α decreases: Comparing Figs. 5 and 10, large η (such as $\eta = 2 \cdot 10^{-4}$) has the least influence when $\alpha = 7$ and the greatest influence when $\alpha = -2$.

To summarize, it can be said that the effect of gravity on the nonlinear modes of the system is significant on the first nonlinear mode, but comparably insignificant on higher-frequency modes. On the first nonlinear mode, it is observed that in a standing configuration ($\alpha > 0$), increasing the effect of gravity serves to *increase* the hardening trend of the backbone, meaning that the global backbone becomes more hardening when taking into account the gravitational field. In a hanging configuration ($\alpha < 0$), the effect is reversed. Interestingly, gravity has an opposite effect on the first *nonlinear* mode as compared to the *linear* one: In the standing configuration, gravity has a hardening effect on the backbone curve of the first nonlinear mode, whereas it has a softening effect on the (linear) natural frequencies, since they decrease as α increases, as described in Sect. 3. A more physical interpretation of

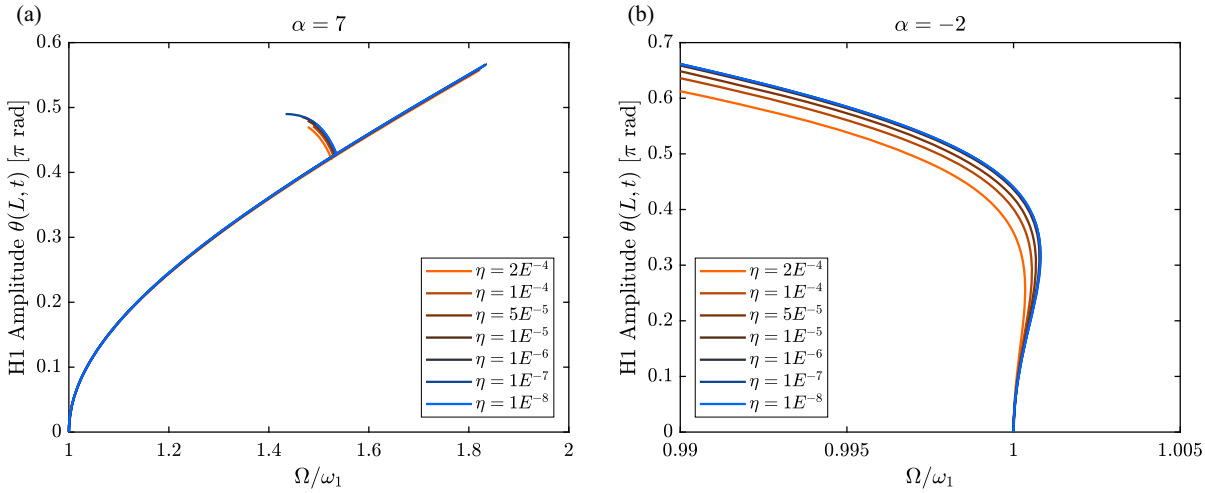

Fig. 10 Effect of dimensionless parameters on the first nonlinear mode, isolation of the effect of η for $\alpha \neq 0$: **a** amplitude of the first harmonic H1 of θ at the free end of the beam for different values of η in the standing configuration ($\alpha = 7$), **b** the same as (a) but in the hanging configuration ($\alpha = -2$)

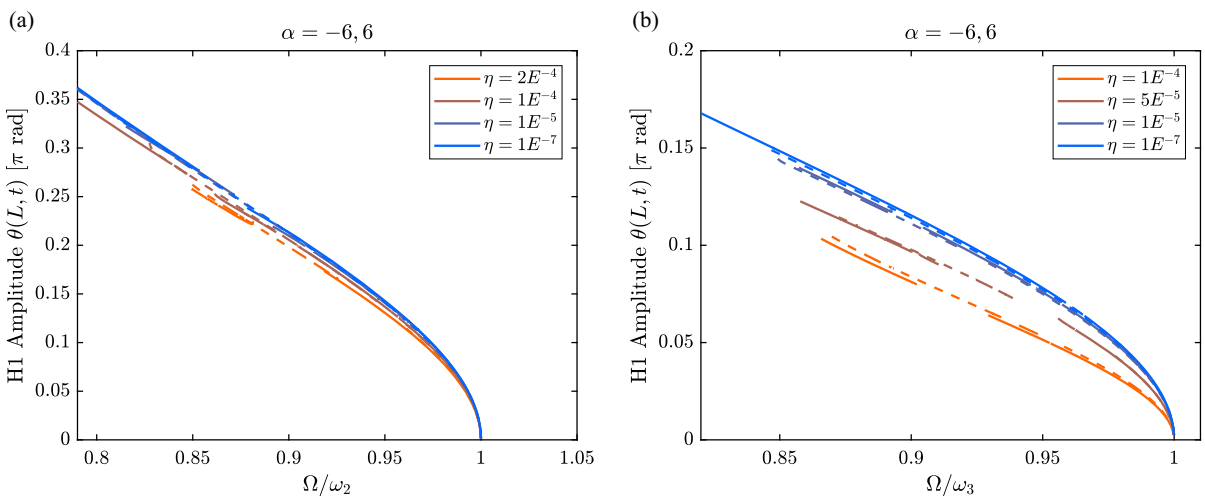

Fig. 11 Effect of dimensionless parameters on the second and third nonlinear modes, isolation of the effect of η for $\alpha \neq 0$: **a** amplitude of the first harmonic H1 of θ at the free end of the beam for different values of η (solid curve: $\alpha = -6$, dotted curve: $\alpha = 6$), **b** the same as **a** but on the third nonlinear mode

these effects is outlined in Sect. 6 using a simple pendulum system.

Finally, it is noted that the case of the hanging configuration is very similar to the case of a rotating cantilever beam, in which the beam is subjected to a centrifugal axial field. In this case, the effect of the centrifugal force is hardening for the (linear) natural frequencies and softening for the backbone curves (see, e.g., [44,62]). The similarity between the two cases can be linked to the axial preload condition, with the only difference being that the load is not uniform (it increases with x) in the case of the rotating beam.

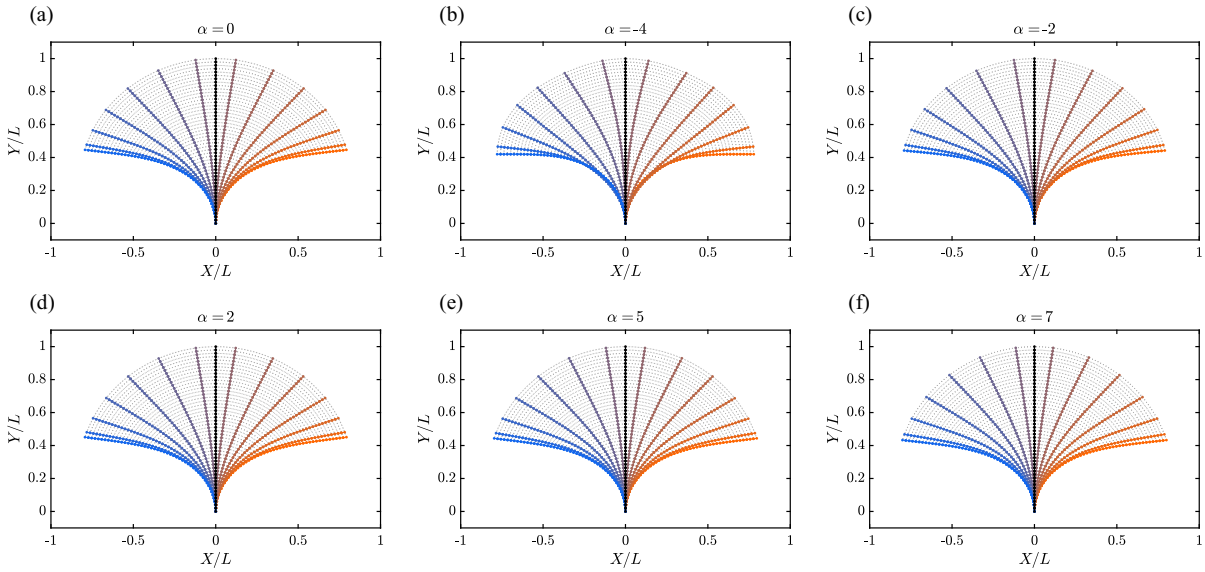

Fig. 12 Snapshots of the cantilever beam vibrating on its first nonlinear mode for different values of α. The locations on the corresponding backbones at which the snapshots are taken are marked by red circles in Fig. 8**a**

5 Nonlinear mode shapes

5.1 Effect of α on the first nonlinear mode shape

In addition to the effect of (α, η) on the nonlinear backbone curves, it is also of interest to study the effect of gravity on the deformed shape in the nonlinear region. Based on the results of Sect. 4, we choose to concentrate the investigation primarily on the influence of α for a chosen $\eta = 10^{-7}$ on the first nonlinear mode, since it is shown in Sects. 3 and 4 that both η (when small) and α do not have a strong influence on the higher-frequency modes up to α_{crit}.

First, we investigate the effect of α on the deformed shape of the beam at moderate-to-high cross-section rotations, around a maximum H1 amplitude of 0.45π rad, considering this region to be representative of moderate-to-high amplitudes of vibration (and, therefore, judiciously considered as nonlinear behavior). This is justified since the analytical backbone computation based on the third-order inextensible beam model of Crespo da Silva et al., recalling the black dashed line in Fig. 5a, begins to diverge from the geometrically exact model around $\theta = 0.2\pi$ rad.

To study the effect of the gravity parameter α on the deformed shape of the beam, the deformed shape is traced at points of (nearly) constant amplitudes along each of the $\alpha \in \{-4, -2, 0, 2, 5, 7\}$ backbones, shown as red circles in Fig. 8a. Since the continuation points are different for each numerical computation, it is not possible to select an exact amplitude of 0.45π rad in all simulations, the closest continuation point being selected instead. The coordinates of the red circles in Fig. 8a for each backbone curve are tabulated in Table 2.

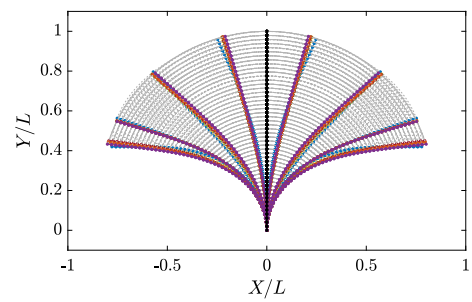

Fig. 13 Snapshots Fig. 12a-f condensed into one figure: $\alpha = 0$ (green), $\alpha = -4$ (blue), $\alpha = -2$ (yellow), $\alpha = 2$ (red), $\alpha = 5$ (orange), $\alpha = 7$ (purple). (Color figure online)

The deformed shapes of the cantilever beam at these points along the backbone curves are gathered in Fig. 12. The deformed shapes are taken as a certain number of snapshots over a fixed time interval equal to half of the period of the periodic motion. Over the half period, the individual snapshots of the deformed shapes appear as the colored curves, the initial refer-

Table 2 Coordinates at which the deformed shapes in Fig. 12 are taken, as shown by the red circles in Fig. 8**a**

α	Ω/ω_1	Amp. H1 θ [π rad]
-4	0.9854	0.4497
-2	0.9998	0.4497
0	1.0179	0.4500
2	1.0469	0.4491
5	1.1590	0.4511
7	1.5814	0.4505

ence (undeformed) configuration is the black curve, and the dashed light gray curves joining the colored curves represent the trajectory of the nodes (see Fig. 12). In addition, the individual snapshots of Fig. 12 are gathered together in a single plot in Fig. 13.

It is immediately observed that the deformed shapes of the beam in Figs. 12 and 13 are nearly indistinguishable despite the points being taken at very different frequencies. For example, the $\alpha = 0$ deformed shape (Fig. 12a) is traced for a frequency of $\Omega/\omega_1 = 1.0179$, while the $\alpha = 7$ deformed shape (Fig. 12f) is traced for a frequency of $\Omega/\omega_1 = 1.5814$, 1.61 times larger, yet the deformed shapes are nearly identical. Between Fig. 12a–f, only the effect of α, i.e., of gravity, changes; comparing Figs. 8 and 12 proves that although changing α bends the backbone curve either more hardening or more softening depending on the sign of α (and, therefore, shifts the frequency higher or lower), *the deformed shape of the nonlinear mode is essentially not influenced by gravity.*

5.2 Evolution of mode shape as a function of the amplitude

The surface plots in Fig. 14 provide another useful visualization for understanding the development of the nonlinear deformed shape of the cantilever for different values of α. Each surface plot corresponds to a backbone curve of Fig. 8a for $\alpha \in \{-2, 0, 5\}$, $\eta = 10^{-7}$. The surfaces depict the amplitude of the first harmonic H1 of the rotation $\theta(x,t)$, normalized by its value at $x = L$, as a function of (1) the cross-section positions $\bar{x} = x/L$ and (2) the amplitude of the first harmonic H1 of the rotation $\theta(L,t)$ at the free end. Consequently, at $x = L$, the amplitude of the surface is exactly 1. The curves are plotted, for each α, for the same range of amplitudes H1 of $\theta(L,t)$ as their backbone counterparts in Fig. 8.

These surface plots can be interpreted as the evolution of the first mode shape of the beam as a function of the amplitude of the motion. To understand this, consider first the case of the linearized model, valid for small amplitude. In this case, the motion on the first mode would be exactly $\theta(x,t) = w'(x,t) = \Phi_1'(x)\cos\Omega t$, with

$$\Phi_i'(x) = \beta_i\left[\sin\beta_i x + \sinh\beta_i x + a_i(\cos\beta_i x - \cosh\beta_i x)\right], \quad i \in \mathbb{N}^*, \tag{29}$$

obtained by differentiating Eq. (47), showing naturally that the deformed shape $\Phi_1'(x)$ of the motion does not depend on the amplitude. The first mode shape $\Phi_1(\bar{x})$ and its derivative $\Phi_1'(\bar{x})$, normalized by their values at $x = L$, are overlaid on top of the surfaces in Fig. 14.

Analyzing Fig. 14, it can be concluded that, similar to a linear system, *the deformed shape of the first (leading) harmonic of the cross-section rotation $\theta(x,t)$ motion on the first nonlinear mode is nearly independent of the motion amplitude*, since the surfaces are almost flat as a function of H1 of $\theta(L,t)$. Since the first harmonic is leading up to large amplitude, this conclusion indicates that the motion can be approximated by:

$$\theta(x,t) = \sum_{i=1}^{+\infty}\Phi_i'(x)q_i(t), \tag{30a}$$

$$= \Phi_1'(x)a_1^{(1)}(\Omega)\cos\Omega t + \left[\sum_{i=1}^{+\infty}\Phi_i'(x)a_i^{(3)}(\Omega)\right]\cos 3\Omega t + \left[\sum_{i=1}^{+\infty}\Phi_i'(x)a_i^{(5)}(\Omega)\right]\cos 5\Omega t + \text{HH}, \tag{30b}$$

$$\simeq \Phi_1'(x)a_1^{(1)}(\Omega)\cos\Omega t, \tag{30c}$$

where $a_i^{(h)}(\Omega)$ is the amplitude of the hth harmonic of the ith modal coordinate $q_i(t)$ and HH stands for "higher harmonics." Above, Eq. (30a) is a standard modal expansion, Eq. (30b) represents a Fourier series decomposition explicitly enforcing the aforementioned conclusion that the deformed shape of the first harmonic is independent of the amplitude, and Eq. (30c) neglects the higher harmonics. This result seems astonishing at first sight since the motion of the beam at

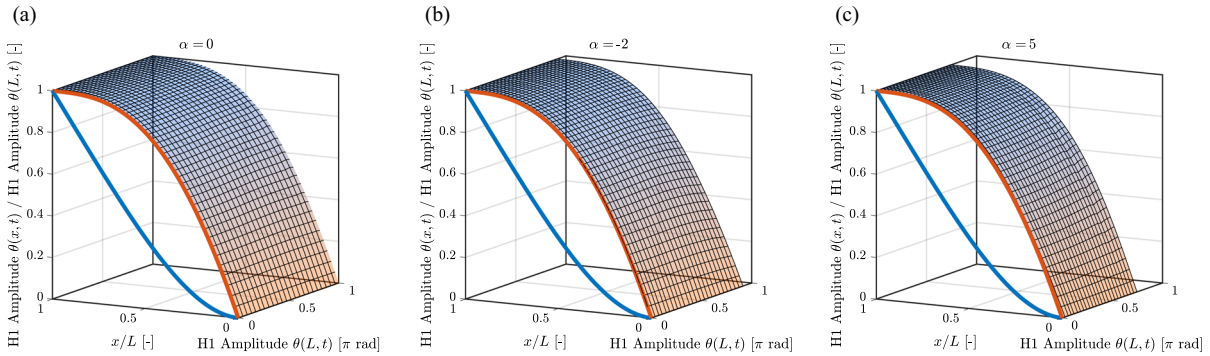

Fig. 14 Surface plots depicting the (normalized) amplitude of H1 of $\theta(x,t)$ as a function of the position $\bar{x} = x/L$ and of the amplitude of H1 of $\theta(L,t)$, for several values of α. These surface plots correspond to the backbones shown in Fig. 8 **a**. In addition, the linear mode shapes $\Phi_1(\bar{x})/\Phi_1(L)$ and $\Phi_1'(\bar{x})/\Phi_1'(L)$ are shown in blue and orange, respectively

high amplitude appears very complex, as observed in Figs. 4a and 12. However, if the motion characterized by $\theta(x,t)$ is *a priori* very simple, the geometrical nonlinearities appear strongly in the displacement fields (u, w) of the points on the centerline of the beam through the kinematics relations (43) (valid if the beam is inextensible), written:

$$w(x,t) = \int_0^x \sin\theta(\xi,t)\,\mathrm{d}\xi \simeq \int_0^x \sin\left[\Phi_1'(\xi)\cos\Omega t\right]\,\mathrm{d}\xi, \tag{31a}$$

$$u(x,t) = \int_0^x (\cos\theta(\xi,t) - 1)\,\mathrm{d}\xi \simeq \int_0^x \left(\cos\left[\Phi_1'(\xi)\cos\Omega t\right] - 1\right)\,\mathrm{d}\xi, \tag{31b}$$

or, in other words, knowing $\theta(x,t)$, it is possible to reconstruct the full two-dimensional motion using Eq. (31).

Then, in order to analyze the effect of the higher harmonics, Figs. 15 and 16 are traced as surfaces depicting the evolution of H3 and H5 on the first nonlinear mode backbone curves in a way analogous to what was done for H1 in Fig. 14**a** for $\alpha = 0$. In Fig. 15, H3 and H5 are normalized by (H3, H5) and by H1 in Fig. 16. Figure 16 explicitly shows that the amplitudes of H3 and H5 are small compared to the amplitude of H1 (a result also visible in Fig. 7), since their amplitudes remain at 10% the amplitude of H1 or below on the entire backbone curve. Moreover, Fig. 15 reveals that although the shapes of harmonics H3 and H5 depend slightly on the amplitude of the motion, the overall shape is close to the second mode shape of the beam, leading to an approximation of $\theta(x,t)$ based on Eq. (30b) as:

$$\theta(x,t) \simeq \Phi_1'(x)a_1^{(1)}(\Omega)\cos\Omega t + \Phi_2'(x)\left(a_2^{(3)}(\Omega)\cos 3\Omega t + a_2^{(5)}(\Omega)\right). \tag{32}$$

Note that the local discontinuities in the H3 and H5 surfaces in Figs. 15 and 16 are related to some internal resonance "offshoots," mentioned in Sect. 4.1. The results presented in this section enable a more deep characterization of the motion on the first nonlinear mode while also laying the groundwork for reduced order modeling of the beam. From this perspective, choosing $\theta(x,t)$ as the principle variable to investigate seems an excellent idea, already pursued in a series of articles [1–3].

Lastly, it is noted that Fig. 14 also demonstrates the independence of the first harmonic of the deformed shape of the beam from gravity, since the shape of Fig. 14a–c remain identical regardless of the value of α.

6 Analogy with a pendulum system

In order to offer a more physical insight into the effect of gravity on both the linear and nonlinear frequencies of the first mode of the cantilever, consider the inverted pendulum of Fig. 17a. The pendulum is of length l, with all of its inertia m concentrated at its tip, and is subjected to a gravitational acceleration **g** and a linear torsional spring of stiffness Γ. The spring is at rest when the pendulum is vertical. For this system, the equation of motion governing the angle θ of the pendulum with

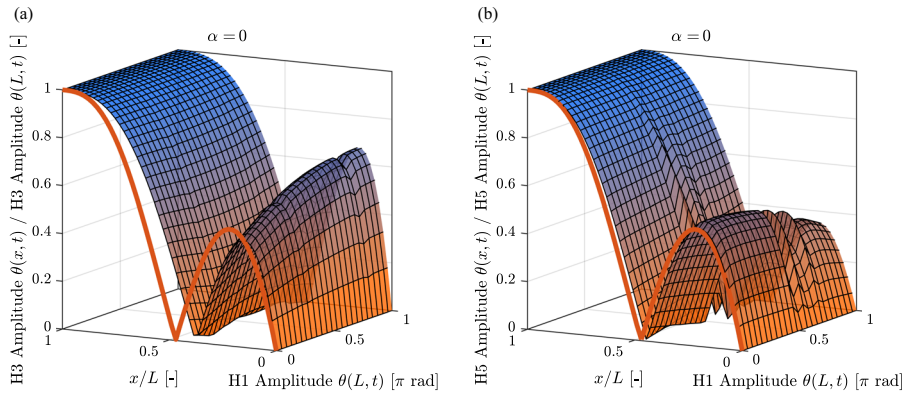

Fig. 15 Surface plots depicting the (normalized) amplitude of H3 or H5 of $\theta(x,t)$ as a function of the position $\bar{x} = x/L$ and of the amplitude of H1 of $\theta(L,t)$: **a** H3, **b** H5. The linear mode shape $\Phi_2'(\bar{x})/\Phi_2'(L)$ is shown in orange

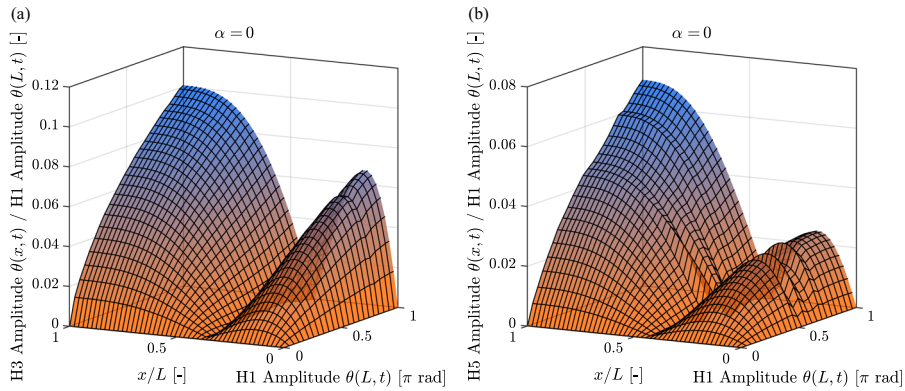

Fig. 16 Surface plots depicting the amplitude of H3 or H5 of $\theta(x,t)$ *normalized by H1* as a function of the position $\bar{x} = x/L$ and of the amplitude of H1 of $\theta(L,t)$: **a** H3, **b** H5

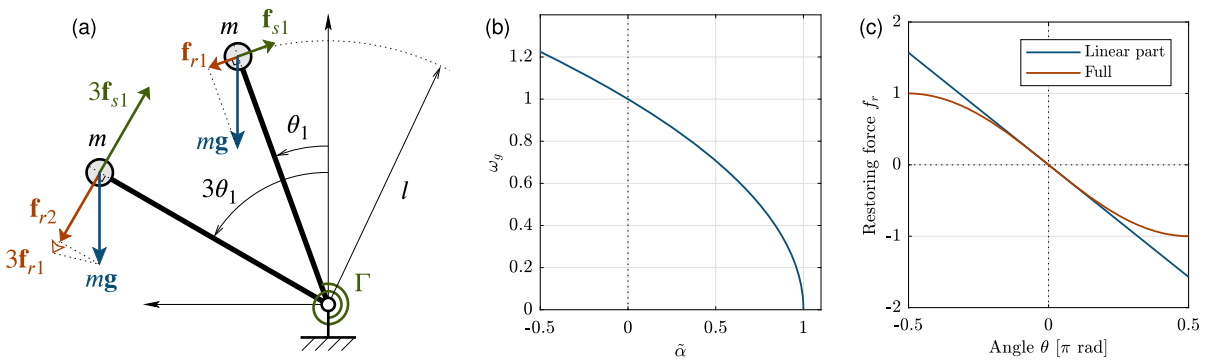

Fig. 17 **a** Pendulum shown in two positions along with restoring force $\mathbf{f}_r$, **b** graph of the natural frequency ω_g of the pendulum as a function of the gravity parameter $\tilde{\alpha}$ (normalized), and **c** graph of the restoring force f_r as a function of angle θ (normalized)

respect to the positive vertical axis can be written:

$$\ddot{\theta} + \frac{\Gamma}{ml^2}\theta - \frac{g}{l}\sin\theta = 0$$
$$\Rightarrow \quad \ddot{\theta} + \omega_0^2(1-\tilde{\alpha})\theta + f_{\mathrm{nl}}(\theta) = 0,$$
$$\omega_0 = \sqrt{\frac{\Gamma}{ml^2}}, \tag{33}$$

where ω_0 is the natural frequency of the pendulum without gravity. In Eq. (33), it is clear that the spring creates a linear restoring force $f_s = \frac{\Gamma}{ml^2}\theta$, while gravity creates a restoring force $f_r = -\frac{g}{l}\sin\theta$ of opposite sign, which works to counteract the restoring force generated by the spring.

Separating the linear part of f_r and denoting by $f_{\mathrm{nl}}(\theta)$ the remaining part, the gravity parameter $\tilde{\alpha}$ and the natural frequency of the pendulum with gravity

$\omega_g(\tilde{\alpha})$ can be defined such that:

$$\tilde{\alpha} = \frac{mlg}{\Gamma}, \quad \omega_g = \omega_0\sqrt{1-\tilde{\alpha}}. \tag{34}$$

In tracing $\omega_g(\tilde{\alpha})$ shown in Fig. 17b, the graph is found to be very similar to that of $\bar{\omega}_1(\alpha)$ for the first mode of the cantilever, shown in Fig. 2b. In the present case of the pendulum, the critical value for self-buckling of the pendulum is $\tilde{\alpha} = 1$. The effect of gravity on the pendulum's natural frequency ω_g is then clear: ω_g decreases as the gravity parameter $\tilde{\alpha}$ increases since it creates a restoring force *opposed to that of the spring*, thereby decreasing the overall stiffness of the pendulum. Gravity, thus, has a *softening linear effect*.

Considering the nonlinear part of the restoring force $f_{nl} = \omega_0^2\tilde{\alpha}(\theta - \sin\theta)$, it appears to add a *positive* nonlinear part to the linear restoring force $-\omega_0^2\tilde{\alpha}\theta$, which explains why gravity has a *hardening nonlinear effect*; it is responsible for a nonlinear frequency that increases with the amplitude of the motion. From a physical point of view, this can be explained by a projection effect of the gravity force $m\mathbf{g}$ in the tangent direction (the direction of the restoring force $\mathbf{f}_s$ of the spring, see Fig. 17a). As θ increases, the "full" $f_r(\theta)$ increases less in absolute value than its "linear part," thus creating a nonlinear effect of opposite nature (hardening) with respect to the linear one (softening). This is illustrated by the graph of Fig. 17c, where the "full" restoring force curve $f_r(\theta)$ is above its "linear part" $-\omega_0^2\tilde{\alpha}\theta$ for $\theta > 0$ and below if $\theta < 0$.

Returning to the case of the cantilever, it can be imagined that the distributed force due to gravity has the same projection effect in each infinitesimal part of the cantilever beam. Since the curvature of the first mode shape is constant along the beam as evidenced in §5, the analogy to the pendulum system holds. In the case of modes 2 and 3 of the cantilever, a double or triple pendulum would likely lead to analogous results.

7 Conclusion

In this work, the influence of gravity on the dynamics of flexible slender cantilevers is studied. The cantilevers are considered to be vertically oriented in either a standing or hanging configuration and are subjected to a gravitational acceleration g. It is found that by normalizing the system by the length of the cantilever, only two dimensionless parameters, a "slenderness" parameter η and a "gravity" parameter α, primarily govern the dynamics of the beam. In the linear region, shown in Sect. 3, it is found that, globally, η holds little influence over the linear natural frequencies $\bar{\omega}_m$ of the first three bending modes $m = 1, 2, 3$, while α holds a much greater influence, particularly on the first mode. In a hanging configuration (represented by $\alpha < 0$), increasing the magnitude of α increases $\bar{\omega}_m$, while increasing the magnitude of α in a standing configuration ($\alpha > 0$) decreases $\bar{\omega}_m$ up to a value of α_{crit}, at which the standing cantilever buckles under its own weight.

At larger amplitudes of vibration, the dynamics of the slender cantilever become nonlinear due to the influence of the geometrical nonlinearities tied to the rotation of the cross sections. In particular, the nonlinear modes, visually represented as backbone curves in a traditional amplitude/frequency plot and as deformed "snapshots" of the structure at high amplitude, are studied, the results of which are shown in Sects. 4 and 5. In the nonlinear region, it is found that, as in the linear region, η globally holds little influence over the first three nonlinear modes, so long as η remains small ($\eta \leq 10^{-5}$ for modes 1 and 2 or $\eta \leq 10^{-6}$ for mode 3). The backbone curves are also validated by an analytical backbone computation based on the inextensible beam model of Crespo da Silva et al., valid up to moderate amplitudes of vibration. Regarding the influence of α, it is found that α has a very large effect on the first nonlinear mode in particular, with much less effect on modes 2 and 3. Increasing the magnitude of α in a standing configuration hardens the backbone of the first nonlinear mode, while increasing the magnitude of α in a hanging configuration softens the backbone. Interestingly, however, the different values of α do not influence the deformed shape of the first nonlinear mode. Finally, α is shown to have very little influence on the higher nonlinear modes 2 and 3. The behavior of the first nonlinear mode under the influence of gravity is interpreted in another context through an analogy to a simple pendulum system in Sect. 6. It is noted, however, that significant difficulties were encountered during computation of some of the backbone curves, particularly on the higher modes, due to the detection of many complex internal resonances (see Sect. 4.1). Further investigation of these internal resonances is required to better understand the nonlinear behavior of the system at these locations.

The results of this work highlight the importance of incorporating gravity in any dynamical simulations, particularly when investigating the first mode of a cantilever beam within a gravitational field. Future studies will aim to compare numerical simulations including consideration of gravity to experimental measurements, in particular of the nonlinear modes, in addition to studying the effects of gravity on different beam orientations (such as a "horizontal" cantilever with gravity perpendicular to the axis of the beam) and types of systems.

Acknowledgements This project has received funding from the European Union's Horizon 2020 research and innovation program under the Marie Skłodowska-Curie grant agreement No. 860124. The present paper only reflects the authors' view. The European Commission and its Research Executive Agency (REA) are not responsible for any use that may be made of the information it contains. The authors would also like to thank Hamed Farokhi from Northumbria University for the idea behind this investigation.

Author contributions Marielle Debeurre provided software and contributed to investigation, visualization, and writing—original draft preparation, review, and editing
Aurélien Grolet was involved in conceptualization, methodology, supervision, and writing—review and editing
Olivier Thomas contributed to conceptualization, methodology, supervision, and writing—review and editing

Funding This project has received funding from the European Union's Horizon 2020 research and innovation program under the Marie Skłodowska-Curie grant agreement No. 860124.

Data availability The data generated and analyzed in this study are available upon request.

Declarations

Conflict of interest The authors declare that they have no known competing financial or non-financial interests that could have appeared to influence this work.

A. Effect of shear parameter μ

As detailed in Sect. 2, a third dimensionless parameter related to the shear stiffness of the beam (which is present exclusively in the case of Timoshenko kinematics), called μ in §2, appears in the equations of motion Eqs. (7) and (8). Recalling Eq. (6), μ is found to depend on three parameters: the shear coefficient k, the Poisson's ratio ν and the slenderness parameter η. Considering only slender beams such that η is very small ($\eta \leq 2 \cdot 10^{-4}$), it naturally follows that μ is also very small, being proportional to η. Recalling Eq. (8), a very small μ tends the overall shear stiffness toward infinity, i.e., to the point of no shearing of the cross section as in Euler–Bernoulli kinematics. Therefore, for very small μ, it can be considered that there is very little effect of shearing of the cross section (even at high amplitudes of rotation) and little difference between Timoshenko and Euler–Bernoulli kinematics.

Table 3 Values of μ for different values of k and ν, with $\eta = 1 \cdot 10^{-7}$

$\mu = \frac{2(1+\nu)\eta}{k}$	k	ν	η
$2.22 \cdot 10^{-7}$	0.9	0.0	
$2.60 \cdot 10^{-7}$	1.0	0.3	$1 \cdot 10^{-7}$
$3.75 \cdot 10^{-7}$	0.8	0.5	

In order to confirm the minor influence of the dimensionless parameter μ, the simulations of Sect. 4 were performed again with different values of k and ν while keeping η and α the same. As mentioned in Sect. 2.2, typical values of k and ν are in the ranges of $0.8 \leq k \leq 0.9$ and $0 \leq \nu \leq 0.5$, respectively. The two extremities of μ within these ranges for k and ν were selected, $\mu = 2.22 \cdot 10^{-7}$ and $3.75 \cdot 10^{-7}$ for $\eta = 1 \cdot 10^{-7}$, in order to compare with the simulations of Sect. 4, where $k = 1$, $\nu = 0.3$. The breakdown of these parameters is shown in Table 3.

The simulations of Sect. 4.1 and 4.2 (where $\mu = 2.60 \cdot 10^{-7}$ for $\eta = 10^{-7}$) are recomputed using these two additional values of μ. For the latter, $\alpha = 5$ is chosen. The results of these simulations are summarized in Fig. 18; the orange curves in both figures are the same as their counterparts in Sect. 4.

In both conditions, regardless of the presence of gravity in Fig. 18b, the variation in μ between its minimum and maximum values has next to no effect on the backbone curve of the first nonlinear mode; the three curves overlap to the point of being indistinguishable. These comparisons prove the negligible influence of shearing on the mechanics of very slender beams and, therefore, justify the omission of the third dimensionless parameter μ from the analyses presented in this work.

B. Tangent stiffness computation

According to Eq. (24), the tangent stiffness $\mathbf{K}_t$ is defined as the first derivative of the internal force

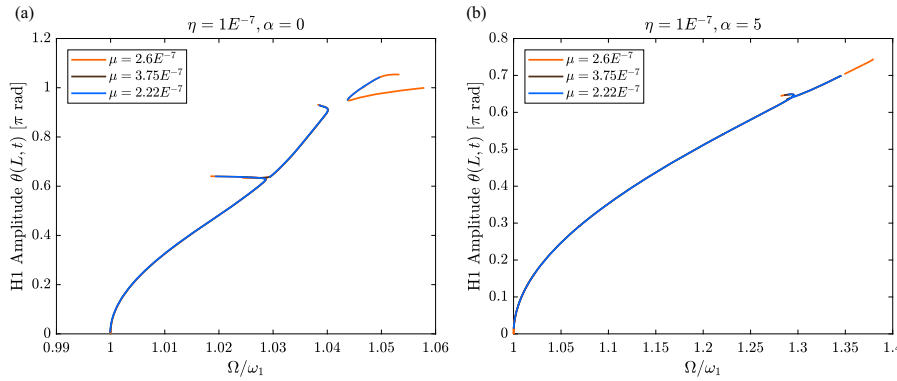

Fig. 18 Effect of dimensionless parameters on the first nonlinear mode, isolation of the effect of μ: **a** amplitude of the first harmonic H1 of θ at the free end of the beam for different values of μ, no-gravity condition ($\alpha = 0$), **b** the same as **a** but with gravity condition ($\alpha = 5$)

vector $\mathbf{f}_{\text{int}}$ with respect to the vector of degrees of freedom:

$$\mathbf{K}_{\text{t}} = \frac{\partial \mathbf{f}_{\text{int}}}{\partial \mathbf{q}}. \tag{35}$$

In practice, it can be computed at the elementary level and then assembled according to standard finite element procedures.

All details having been explained in previous work [4,44], we recall here only the main parts of the reasoning. First, the strains of Eq. (2) are discretized according to Eq. (12), yielding the elementary strain expressions:

$$e^e = \left(1 + \frac{u_2 - u_1}{L^e}\right)\cos\theta^e + \left(\frac{w_2 - w_1}{L^e}\right)\sin\theta^e - 1, \tag{36a}$$

$$\gamma^e = \left(\frac{w_2 - w_1}{L^e}\right)\cos\theta^e - \left(1 + \frac{u_2 - u_1}{L^e}\right)\sin\theta^e, \tag{36b}$$

$$\kappa^e = \frac{\theta_2 - \theta_1}{L^e}. \tag{36c}$$

Then, the elementary discretized gradient matrix is defined as:

$$\delta\boldsymbol{\varepsilon}^e = \mathbf{B}^e \delta\mathbf{q}^e$$
$$\Rightarrow \quad \mathbf{B}^e = \frac{1}{L_e}\begin{bmatrix} -\cos\theta^e & -\sin\theta^e & N_1(x)L^e\gamma^e & \cos\theta^e & \sin\theta^e & N_2(x)L^e\gamma^e \\ \sin\theta^e & -\cos\theta^e & -N_1(x)L^e(1+e^e) & -\sin\theta^e & \cos\theta^e & -N_2(x)L^e(1+e^e) \\ 0 & 0 & -1 & 0 & 0 & 1 \end{bmatrix}, \tag{37}$$

with $\boldsymbol{\varepsilon}^e = [e^e \ \gamma^e \ \kappa^e]^{\text{T}}$. Considering the internal virtual work (see [4,44]), the elementary internal force vector is written:

$$\mathbf{f}^e_{\text{int}}(\mathbf{q}^e) = \int_0^{L^e} (\mathbf{B}^e)^{\text{T}} \mathbf{C}\boldsymbol{\varepsilon}^e \, \text{d}x, \tag{38}$$

with:

$$\mathbf{C} = \begin{bmatrix} EA & 0 & 0 \\ & kGA & 0 \\ & & EI \end{bmatrix}. \tag{39}$$

Recalling Eqs. (35) and (36), the first variation of Eq. (38) can be written:

$$\delta\mathbf{f}^e_{\text{int}}(\mathbf{q}^e) = \left\{ \int_0^{L^e} (\mathbf{B}^e)^{\text{T}} \mathbf{C}\mathbf{B}^e \, \text{d}x + \int_0^{L^e} \left(\frac{\partial \mathbf{B}^e}{\partial \mathbf{q}^e}\right)^{\text{T}} \mathbf{C}\boldsymbol{\varepsilon}^e \, \text{d}x \right\} \delta\mathbf{q}^e = \mathbf{K}^e_{\text{t}} \delta\mathbf{q}^e, \tag{40}$$

where $\mathbf{K}^e_{\text{t}}$ is the elementary tangent stiffness matrix. Finally, $\mathbf{K}^e_{\text{t}}$ is computed $\mathbf{K}^e_{\text{t}} = \mathbf{K}^e_e + \mathbf{K}^e_\gamma + \mathbf{K}^e_\kappa$, with

$$\mathbf{K}_e^e = \frac{EA}{L^e}\begin{bmatrix} K_1 & K_3 & K_4 & -K_1 & -K_3 & K_4 \\ & K_2 & K_5 & -K_3 & -K_2 & K_5 \\ & & K_6 & -K_4 & -K_5 & K_6 \\ & & & K_1 & K_3 & -K_4 \\ & & & & K_2 & -K_5 \\ & & & & & K_6 \end{bmatrix}, \tag{41a}$$

$$\mathbf{K}_\gamma^e = \frac{kGA}{L^e}\begin{bmatrix} K_2 & -K_3 & K_7 & -K_2 & K_3 & K_7 \\ & K_1 & K_8 & K_3 & -K_1 & K_8 \\ & & K_9 & -K_7 & -K_8 & K_9 \\ & & & K_2 & -K_3 & -K_7 \\ & & & & K_1 & -K_8 \\ & & & & & K_9 \end{bmatrix}, \tag{41b}$$

$$\mathbf{K}_\kappa^e = \frac{EI}{L^e}\begin{bmatrix} 0 & 0 & 0 & 0 & 0 & 0 \\ & 0 & 0 & 0 & 0 & 0 \\ & & 1 & 0 & 0 & -1 \\ & & & 0 & 0 & 0 \\ & & & & 0 & 0 \\ & & & & & 1 \end{bmatrix}, \tag{41c}$$

and with:

$$K_1 = \cos^2\bar{\theta}, \quad K_2 = \sin^2\bar{\theta}, \quad K_3 = \cos\bar{\theta}\sin\bar{\theta},$$
$$K_4 = \frac{L^e}{2}(\bar{e}^e\sin\bar{\theta} - \bar{\gamma}^e\cos\bar{\theta}),$$
$$K_5 = -\frac{L^e}{2}(\bar{e}^e\cos\bar{\theta} + \bar{\gamma}^e\sin\bar{\theta}),$$
$$K_6 = \frac{(L^e)^2}{4}\left[(\bar{\gamma}^e)^2 - \bar{e}^e(\bar{e}^e+1)\right],$$
$$K_7 = \frac{L^e}{2}[\bar{\gamma}^e\cos\bar{\theta} - \sin\bar{\theta}(\bar{e}^e+1)],$$
$$K_8 = \frac{L^e}{2}[\bar{\gamma}^e\sin\bar{\theta} + \cos\bar{\theta}(\bar{e}^e+1)],$$
$$K_9 = \frac{(L^e)^2}{4}\left[(\bar{e}^e+1)^2 - (\bar{\gamma}^e)^2\right].$$

In the above expressions for K_i, $i = 1,\dots 9$, $\bar{\theta} = (\theta_1+\theta_2)/2$, $\bar{e} = e(\bar{\theta})$, and $\bar{\gamma} = \gamma(\bar{\theta})$ since the internal force vector integration is evaluated using a single-point Gaussian quadrature at $x = L^e/2$ to avoid shear locking (see [4,44,49]). Then, $\mathbf{K}_\mathrm{t}^e$ is assembly according to standard finite element procedures in order to obtain the full tangent stiffness matrix $\mathbf{K}_\mathrm{t}$.

Notice that $\mathbf{K}_\mathrm{t}^e = \mathbf{K}_\mathrm{t}^e(\mathbf{q}^e)$ and, by extension, $\mathbf{K}_\mathrm{t} = \mathbf{K}_\mathrm{t}(\mathbf{q})$ depend on the degrees of freedom u_i, w_i and θ_i through their presence in $\bar{\theta}$, $\bar{e}$ and $\bar{\gamma}$ (see Eq. (36)); in other words, due to the presence of geometrical nonlinearities, the tangent stiffness of the structure is a function of its deformed state. This serves to explain the dependence of the natural frequencies of the cantilever on the gravitational field, as seen in Eq. (26) and Sect. 3.

As explained in Sect. 2.4, the tangent stiffness matrix is also used in computing the equilibrium solution $\mathbf{q}_\mathrm{s}$ of the cantilever subjected to the gravitational field. In this case, the tangent stiffness is evaluated at $\mathbf{q} = \mathbf{0}$, such that the elementary tangent stiffness prior to assembly takes the form of Eq. (41) with $\mathbf{q}^e = \mathbf{0} \Rightarrow u_1 = u_2 = w_1 = w_2 = \theta_1 = \theta_2 = 0 \Rightarrow \bar{\theta} = e^e = \gamma^e = 0$, which is with $K_1 = 1$, $K_2 = K_3 = K_4 = K_5 = K_6 = K_7 = 0$, $K_8 = L^e/2$ and $K_9 = (L^e)^2/4$.

C. Analytical backbone computation with the third-order inextensible beam model

In this appendix, additional details are provided regarding the approximate inextensible cantilever beam model first introduced by Crespo da Silva et al. in [26,27], serving in Sect. 4 (represented as the black dashed lines in Figs. 5 and 9) as a comparison to the geometrically exact finite element model. This model is very interesting as it is both analytical and valid up to a moderate (but not inconsiderable) amplitude of vibration and has thus been used widely in the literature on nonlinear beam dynamics [54,63]. In our case, it is advantageous to use this model for comparison since, when restricting the modal projection to a single mode and solving via a first-order harmonic balance, the computation of the backbone curve itself becomes analytical.

The derivation of the full inextensible beam model is shown in detail in Section 3.2 of [44], which we use as the starting point for our development. We begin with the strong form of the geometrically exact model, Eq. (3), to which four assumptions are added:

1. The condition of inextensibility;
2. Euler–Bernoulli kinematics along with elimination of the rotatory inertia;
3. Truncation of the geometrical nonlinearities up to order 3 in w;
4. A free end boundary condition.

Based on assumptions 1 and 2, $e = \gamma = 0$, so that Eq. (3c), taking into account the constitutive Eqs. (4), simplifies to $T = -M' - q = -EI\theta'' - q$. Then, eliminating N in Eq. (3b) using (3a) and assumption 4

$(N(L,t) = T(L,t) = 0\ \forall t)$, the following partial differential equation is obtained:

$$\rho A\ddot{w} + \left(\frac{EI\theta'' + q}{\cos\theta}\right)' - \left[\tan\theta \int_L^x (\rho A\ddot{u} - n)\ \mathrm{d}x\right]' = p. \tag{42}$$

To recover the model of Crespo da Silva et al., we first assume no external axial load ($n = 0$) or moment ($q = 0$). Then, the inextensibility condition, written explicitly as $\sqrt{(1+u')^2 + w'^2} - 1 = 0$ [44], is used in order to rewrite the axial displacement as a function of w in Eq. (42) according to $u' = \sqrt{1 - w'^2} - 1$. In addition, the geometrically exact kinematics of the beam with the inclusion of the inextensibility condition simplify to:

$$\sin\theta = w', \qquad \cos\theta = 1 + u' = \sqrt{1 - w'^2}. \tag{43}$$

Finally, performing a Taylor expansion up to order three in w leads to:

$$\rho A\ddot{w} + EI\left(w'''' + w'w''^2 + w'''w'^2\right)' + \frac{\rho A}{2}\left[w' \int_L^x \frac{\partial^2}{\partial t^2}\left(\int_0^x w'^2 \mathrm{d}x\right)\mathrm{d}x\right]' = p. \tag{44}$$

The same normalization as that of Sect. 2 (Eq. (6)) is carried out, so that Eq. (44) becomes:

$$\ddot{\bar{w}} + \bar{w}'''' + \left(\bar{w}'\bar{w}''^2 + \bar{w}'''\bar{w}'^2\right)' + \frac{1}{2}\left[\bar{w}' \int_1^{\bar{x}} \frac{\partial^2}{\partial \bar{t}^2}\left(\int_0^{\bar{x}} \bar{w}'^2 \mathrm{d}\bar{x}\right)\mathrm{d}\bar{x}\right]' = \bar{p}, \tag{45}$$

where all terms are now dimensionless.

Next, the model is discretized via a projection of the transverse displacement w onto a single eigenmode $\Phi_k(x)$, for a given $k \in \mathbb{N}$:

$$\bar{w}(\bar{x}, t) = \Phi_k(\bar{x}) q_k(t), \tag{46}$$

where $q_k(t)$ are the modal coordinates and the transverse mode shapes Φ_k represent those of a cantilever beam, solutions of the linear part of the equations of motion, i.e., $\Phi'''' + \beta^4\Phi = 0$ with boundary conditions $\Phi(0) = \Phi'(0) = \Phi''(1) = \Phi'''(1) = 0$. Written explicitly:

$$\Phi_k(\bar{x}) = \cos\beta_k\bar{x} - \cosh\beta_k\bar{x} - a_k\left(\sin\beta_k\bar{x} - \sinh\beta_k\bar{x}\right). \tag{47}$$

In Eq. (47), the coefficients β_k are related to the dimensionless natural frequencies, such that $\bar{\omega}_k = \beta_k^2$ [50], and the coefficient a_k can be calculated by normalizing the mode shapes Φ_k such that $\int_0^1 \Phi_k^2 \mathrm{d}\bar{x} = 1$. The values of β_k and a_k for the first three bending modes are shown in Table 4.

In a standard procedure, the modal projection (46) is injected into Eq. (45), and the result is multiplied by $\Phi_k(\bar{x})$ and integrated over the length of the beam. Additionally, as we are here deriving an expression for the nonlinear modes/backbone curve (i.e., the *free* and *undamped* solution), the damping terms and external forcing are removed, so that Eq. (45) after the modal projection becomes:

$$\ddot{q}_k + \bar{\omega}_k^2 q_k + \Gamma_k q_k^3 + \Pi_k\left(\ddot{q}_k q_k + \dot{q}_k^2\right) q_k = 0, \tag{48}$$

with:

$$\begin{cases} \Gamma_k = \displaystyle\int_0^1 \left(\Phi_k'\Phi_k''\Phi_k'' + \Phi_k'''\Phi_k'\Phi_k'\right)' \Phi_k \mathrm{d}\bar{x}, & \text{(49a)} \\ \Pi_k = \displaystyle\int_0^1 \left[\Phi_k' \int_1^{\bar{x}} \int_0^{\bar{x}} \Phi_k'\Phi_k' \mathrm{d}\bar{x}\mathrm{d}\bar{x}\right]' \Phi_k \mathrm{d}\bar{x}, & \text{(49b)} \end{cases}$$

where the expressions for Γ_k and Π_k have been evaluated for the first three bending modes based on Eq. (47) and are shown in Table 4.

Next, we seek to solve Eq. (48) using a harmonic balance (HBM) expansion truncated to a single harmonic: $q_k(t) = Q_k \cos\Omega t$ with Q_k the amplitude of the oscillation. Injecting this expression for $q_k(t)$ into Eq. (48) and keeping only terms in $\cos\Omega t$ lead to the analytical expression for the amplitude Q_k as a function of the frequency Ω and thus of the backbone curve:

$$Q_k = 2\sqrt{\frac{\Omega^2 - \omega_k^2}{3\Gamma_k - 2\Omega^2\Pi_k}}. \tag{50}$$

Finally, the dimensionless transverse displacement is recovered according to Eq. (46) restricted to one mode as $\bar{w}(\bar{x}, t) = \Phi_k(\bar{x}) Q_k \cos\Omega t$. The black dashed backbone curve in Fig. 5b is traced by sweeping its amplitude $\Phi_k(1)Q_k(\Omega)$ as a function of Ω. Then, $\bar{w}$ is used to compute the amplitudes of the cross-section rotation according to Eq. (43): $\theta(\bar{x}, t) = \sin^{-1}[\bar{w}'(\bar{x}, t)]$. To trace the analytical black dashed

Table 4 Bending parameters of the k-th bending mode for the first three bending modes of a cantilever beam

k-the bending mode	β_k	a_k	Γ_k	Π_k
1	1.875	0.7341	40.441	4.597
2	4.694	1.0185	13418	144.726
3	7.855	0.9992	269710	1006.43

curves in Figs. 5a and 6 in θ, the first harmonic of $\theta(1,t)$ is computed as the amplitude of the first Fourier coefficient of $\sin^{-1}[\Phi_k(1)Q_k(\Omega)\cos\Omega t]$. It is noted that this Fourier coefficient necessarily has an amplitude less than $\simeq 0.4\pi$ rad due to the limitations of the inverse sine function itself, limiting in turn the maximum amplitude of $\theta(L,t)$ plotted in Figs. 5a and 6.

References

1. Farokhi, H., Xia, Y., Erturk, A.: Experimentally validated geometrically exact model for extreme nonlinear motions of cantilevers. Nonlinear Dyn. **107**, 457–475 (2022)
2. Farokhi, H., Ghayesh, M.H.: Geometrically exact extreme vibrations of cantilevers. Int. J. Mech. Sci. **168**, 105051 (2020)
3. Ghayesh, M.H., Farokhi, H.: Extremely large dynamics of axially excited cantilevers. Thin Walled Struct. **154**, 106275 (2020)
4. Debeurre, M., Grolet, A., Cochelin, B., Thomas, O.: Finite element computation of nonlinear modes and frequency response of geometrically exact beam structures. J. Sound Vib. **548**, 117534 (2023)
5. Greenhill, A.G.: Determination of the greatest height consistent with stability that a vertical pole or mast can be made, and the greatest height to which a tree of given proportions can grow. Proc. Camb. Philos. Soc. **4**, 65–73 (1881)
6. Paidoussis, M.P., Des Trois Maisons, P.E.: Free vibration of a heavy, damped, vertical cantilever. J. Appl. Mech. **38**(2), 524–526 (1971)
7. Schäfer, B.: Free vibrations of a gravity-loaded clamped-free beam. Ingenieur-Archiv. **55**, 66–80 (1985)
8. Yokoyama, T.: Vibrations of a hanging Timoshenko beam under gravity. J. Sound Vib. **141**(2), 245–258 (1990)
9. Naguleswaran, S.: Vibration of a vertical cantilever with and without axial freedom at clamped end. J. Sound Vib. **146**(2), 191–198 (1991)
10. Naguleswaran, S.: Transverse vibration of an uniform Euler–Bernoulli beam under linearly varying axial force. J. Sound Vib. **275**, 47–57 (2004)
11. Bokaian, A.: Natural frequencies of beams under compressive axial loads. J. Sound Vib. **126**(1), 49–65 (1988)
12. Bokaian, A.: Natural frequencies of beams under tensile axial loads. J. Sound Vib. **142**(3), 481–498 (1990)
13. Abramovich, H.: Free vibrations of gravity loaded composite beams. Compos. Struct. **23**, 17–26 (1993)
14. Xi, L.-Y., Li, X.-F., Tang, G.-J.: Free vibration of standing and hanging gravity-loaded Rayleigh cantilevers. Int. J. Mech. Sci. **66**, 233–238 (2013)
15. Hijmissen, J.W., van Horssen, W.T.: On transverse vibrations of a vertical Timoshenko beam. J. Sound Vib. **314**, 161–179 (2008)
16. Virgin, L.N., Plaut, R.H.: Postbuckling and vibration of linearly elastic and softening columns under self-weight. Int. J. Solids Struct. **41**, 4989–5001 (2004)
17. Virgin, L.N., Santillan, S.T., Holland, D.B.: Effect of gravity on the vibration of vertical cantilevers. Mech. Res. Commun. **34**, 312–317 (2007)
18. Santillan, S.T., Plaut, R.H., Witelski, T.P., Virgin, L.N.: Large oscillations of beams and columns including self-weight. Int. J. Non-Linear Mech. **43**, 761–771 (2008)
19. Luongo, A., Rega, G., Vestroni, F.: On nonlinear dynamics of planar shear indeformable beams. J. Appl. Mech. **53**, 619–624 (1986)
20. Farokhi, H., Kohtanen, E., Erturk, A.: Extreme parametric resonance oscillations of a cantilever: an exact theory and experimental validation. Mech. Syst. Signal Process. **196**, 110342 (2023)
21. Reissner, E.: On one-dimensional finite-strain beam theory: the plane problem. J. Appl. Math. Phys. **23**, 795–804 (1972)
22. Reissner, E.: On finite deformations of space-curved beams. J. Appl. Math. Phys. **32**, 734–744 (1981)
23. Simo, J.C.: A finite strain beam formulation. The three-dimensional dynamic problem. Part I. Comput. Methods Appl. Mech. Eng. **49**, 55–70 (1985)
24. Le Marrec, L., Lerbet, J., Rakotomanana, L.R.: Vibration of a Timoshenko beam supporting arbitrary large pre-deformation. Acta Mech. **229**, 109–132 (2018)
25. Meier, C., Popp, A., Wall, W.A.: Geometrically exact finite element formulations for slender beams: Kirchhoff-love theory versus Simo-Reissner theory. Arch. Comput. Methods Eng. **26**, 163–243 (2019)
26. Crespo da Silva, M.R.M., Glynn, C.C.: Nonlinear flexural-flexural-torsional dynamics of inextensible beams. I. Equations of motion. J. Struct. Mech. **6**, 437–448 (1978)
27. Crespo da Silva, M.R.M., Glynn, C.C.: Nonlinear flexural-flexural-torsional dynamics of inextensible beams. II. Forced motions. J. Struct. Mech. **6**, 449–461 (1978)
28. Damil, N., Potier-Ferry, M.: A new method to compute perturbed bifurcation: application to the buckling of imperfect elastic structures. Int. J. Eng. Sci. **26**, 943–957 (1990)
29. Cochelin, B., Damil, N., Potier-Ferry, M.: Asymptotic-numerical method and Padé approximations for non-linear

elastic structures. Int. J. Numer. Meth. Eng. **37**, 1187–1213 (1994)
30. Cochelin, B., Vergez, C.: A high order purely frequency-based harmonic balance formulation for continuation of periodic solutions. J. Sound Vib. **324**(1–2), 243–262 (2009)
31. Karkar, S., Cochelin, B., Vergez, C.: A high-order, purely frequency based harmonic balance formulation for continuation of periodic solutions: the case of non-polynomial nonlinearities. J. Sound Vib. **332**(4), 968–977 (2013)
32. Guillot, L., Lazarus, A., Thomas, O., Vergez, C., Cochelin, B.: A purely frequency based Floquet–Hill formulation for the efficient stability computation of periodic solutions of ordinary differential systems. J. Comput. Phys. **416**, 109477 (2020)
33. Leyendecker, S., Betsch, P., Steinmann, P.: Objective energy-momentum conserving integration for the constrained dynamics of geometrically exact beams. Comput. Methods Appl. Mech. Eng. **195**, 2313–2333 (2006)
34. Lang, H., Linn, J., Arnold, M.: Multi-body dynamics simulation of geometrically exact Cosserat rods. Multibody Syst. Dyn. **25**, 285–312 (2011)
35. Brüls, O., Cardona, A., Arnold, M.: Lie group generalized-α time integration of constrained flexible multibody systems. Mech. Mach. Theory **48**, 121–137 (2012)
36. Sonneville, V., Cardona, A., Brüls, O.: Geometrically exact beam finite element formulated on the special Euclidean group SE(3). Comput. Methods Appl. Mech. Eng. **268**, 451–474 (2014)
37. Rong, J., Wu, Z., Liu, C., Brüls, O.: Geometrically exact thin-walled beam including warping formulated on the special Euclidean group se(3). Comput. Methods Appl. Mech. Eng. **369**, 113062 (2020)
38. Touzé, C., Vizzaccaro, A., Thomas, O.: Model order reduction methods for geometrically nonlinear structures—a review of nonlinear techniques. Nonlinear Dyn. **105**, 1141–1190 (2021)
39. Nayfeh, A.H., Mook, D.T.: Nonlinear Oscillations. John Wiley, New York (1995)
40. Shami, Z.A., Giraud-Audine, C., Thomas, O.: A nonlinear piezoelectric shunt absorber with a 2:1 internal resonance: theory. Mech. Syst. Signal Process. **170**, 108768 (2022)
41. Guillot, L., Vigué, P., Vergez, C., Cochelin, B.: Continuation of Quasi-periodic solutions with two-frequency Harmonic Balance method. J. Sound Vib. **394**, 434–450 (2017)
42. Farokhi, H., Erturk, A.: Three-dimensional nonlinear extreme vibrations of cantilevers based on a geometrically exact model. J. Sound Vib. **510**, 116295 (2021)
43. Kerschen, G., Peeters, M., Golinval, J.C., Vakakis, A.F.: Nonlinear normal modes, Part I: a useful framework for the structural dynamicist. Mech. Syst. Signal Process. **23**, 170–194 (2009)
44. Thomas, O., Sénéchal, A., Deü, J.-F.: Hardening and softening behavior and reduced order modeling of nonlinear vibrations of rotating cantilever beams. Nonlinear Dyn. **86**, 1293–1318 (2016)
45. Ogden, R.W.: Non-Linear Elastic Deformations. Dover, New York (1997)
46. Föppl, A. (1897) Vorlesungen über Technische Mechanik. Dritter Band Festigkeitslehre. Druck & Verlag von B. G. Teubner, Leipzig
47. Kaneko, T.: On Timoshenko's correction for shear in vibrating beams. J. Phys. D Appl. Phys. **8**, 1927–1936 (1975)
48. Renton, J.D.: Generalized beam theory applied to shear stiffness. Int. J. Solids Struct. **27**(15), 1955–1967 (1991)
49. Felippa, C.: Nonlinear Finite Element Methods, chapter 9: The TL Timoshenko Plane Beam Element. University of Colorado, Boulder (2001)
50. Géradin, M., Rixen, D.: Mechanical Vibrations. Theory and Application to Structural Dynamics. Wiley, New York (1997)
51. Neukirch, S., Frelat, J., Goriely, A., Maurini, C.: Vibrations of post-buckled rods: the singular inextensible limit. J. Sound Vib. **331**, 704–720 (2012)
52. Neukirch, S., Goriely, A., Thomas, O.: Singular inextensible limit in the vibrations of post-buckled rods: analytical derivation and role of boundary conditions. J. Sound Vib. **333**(3), 962–970 (2014)
53. Neukirch, S., Yavari, M., Challamel, N., Thomas, O.: Comparison of the von Kármán and Kirchhoff models for the post-buckling and vibrations of elastic beams. J. Theor., Comput. Appl. Mech., (May 2021). https://jtcam.episciences.org/7500
54. Nayfeh, A.H., Paï, P.F.: Linear and Nonlinear Structural Mechanics. John Wiley, New York (2004)
55. Givois, A., Grolet, A., Thomas, O., Deü, J.-F.: On the frequency response computation of geometrically nonlinear flat structures using reduced-order finite element models. Nonlinear Dyn. **97**(2), 1747–1781 (2019)
56. Touzé, C., Camier, C., Favraud, G., Thomas, O.: Effect of imperfections and damping on the type of nonlinearity of circular plates and shallow spherical shells. Math. Probl. Eng. **678307**, 2008 (2008)
57. Camier, C., Touzé, C., Thomas, O.: Non-linear vibrations of imperfect free-edge circular plates and shells. Eur. J. Mech. A/ Solids **28**(3), 500–515 (2009)
58. Vizzaccaro, A., Opreni, A., Salles, L., Frangi, A., Touzé, C.: High order direct parametrisation of invariant manifolds for model order reduction of finite element structures: application to large amplitude vibrations and uncovering of a folding point. Nonlinear Dyn. **110**(1), 525–571 (2022)
59. Marconi, J., Tiso, P., Quadrelli, D.E., Braghin, F.: A higher-order parametric nonlinear reduced-order model for imperfect structures using Neumann expansion. Nonlinear Dyn. **104**, 3039–3063 (2021)
60. Qiao, W., Guo, T., Kang, H., Zhao, Y.: Softening-hardening transition in nonlinear structures with an initial curvature: a refined asymptotic analysis. Nonlinear Dyn. **107**, 357–374 (2022)
61. Sun, X., Kerschen, G., Cheng, L.: Geometrical nonlinearities in a curved cantilever beam: a condensation model and inertia-induced nonlinear features. Nonlinear Dyn. **111**, 6533–6556 (2023)

62. Martin, A., Opreni, A., Vizzaccaro, A., Debeurre, M., Salles, L., Frangi, A., Thomas, O., Touzé, C.: Reduced order modeling of geometrically nonlinear rotating structures using the direct parametrisation of invariant manifolds. J. Theor., Comput. Appl. Mech., 2023. submitted, https://hal.science/hal-03886793
63. Colin, M., Thomas, O., Grondel, S., Cattan, E.: Very large amplitude vibrations of flexible structures: experimental identification and validation of a quadratic drag damping model. J. Fluids Struct. **97**, 103056 (2020)